

Effects of Cloud-Radiative Heating on AGCM Simulations of Convectively Coupled Equatorial Waves

Jia-Lin Lin¹, Daehyun Kim², Myong-In Lee³, and In-Sik Kang²

¹NOAA ESRL/CIRES Climate Diagnostics Center, Boulder, CO

²School of Earth and Environmental Sciences, Seoul National University, Seoul, Korea

³NASA GSFC Global Modeling and Assimilation Office, Greenbelt, MD

J. Geophys. Res.

Revised, June 2007

Corresponding author address: Dr. Jia-Lin Lin
NOAA ESRL/CIRES Climate Diagnostics Center
325 Broadway, R/PSD1, Boulder, CO 80305-3328
Email: jjalin.lin@noaa.gov

1 **Abstract**

2 This study examines the effects of cloud-radiative heating on convectively coupled
3 equatorial waves simulated by the Seoul National University (SNU) atmospheric general
4 circulation model (AGCM). The strength of cloud-radiative heating is adjusted by
5 modifying the autoconversion rate needed for cloud condensates to grow up to rain drops.
6 The results show that increasing the autoconversion rate has little effect on the
7 climatological mean precipitation, but it significantly reduces the time-mean clouds and
8 radiative heating in the upper troposphere and enhances heating due to moist processes in
9 the middle troposphere. These lead to cooling of time-mean upper troposphere
10 temperature and drying of lower troposphere moisture. Reduction of cloud-radiative
11 heating enhances the prominence of Kelvin and $n=0$ eastward inertial gravity (EIG)
12 waves. It also tends to enhance significantly the variance of the Kelvin, equatorial Rossby
13 (ER), mixed Rossby-gravity (MRG) and $n=1$ westward inertial gravity (WIG) waves, but
14 not the Madden-Julian Oscillation (MJO) or $n=0$ EIG wave. Reduction of cloud-radiative
15 heating has little effect on the phase speed of the waves, which is associated with
16 unchanged effective static stability caused by the near cancellation between reduced dry
17 static stability and reduced diabatic heating.

18 An important implication of this study is that when tuning GCM's top-of-the-
19 atmosphere radiative fluxes to fit the observations, one needs to make sure that the
20 enhancement factor of cloud-radiative heating at the intraseasonal time-scale also fit with
21 the observation so that the convectively coupled equatorial waves are not suppressed.

1. Introduction

The tropical deep convection does not occur randomly, but is often organized by convectively coupled equatorial waves, such as the Madden-Julian Oscillation (Madden and Julian 1971), Kelvin, equatorial Rossby (ER), mixed Rossby-gravity (MRG), and eastward inertio-gravity (EIG) and westward inertio-gravity (WIG) waves (e.g. Takayabu 1994; Wheeler and Kiladis 1999, hereafter WK). These waves significantly affect a wide range of tropical weather such as the onset and breaks of the Indian and Australian summer monsoons (e.g. Yasunari 1979; Wheeler and McBride 2005), and the formation of tropical cyclones in almost all basins (e.g. Liebmann et al. 1994; Maloney and Hartmann 2001a; Bessafi and Wheeler 2006). On a longer timescale, the convectively coupled equatorial waves also trigger or terminate some El Nino events (e.g. Kessler et al. 1995, Takayabu et al. 1999, Bergman et al. 2001; Roundy and Kiladis 2006). Therefore, these waves are important for both weather prediction and climate prediction.

Unfortunately, these convectively coupled equatorial waves are not well simulated in the general circulation models (GCMs) used for predictions and projections. For example, poor simulation of the MJO has been a well-known long-standing problem in GCMs, and the model MJOs are often too weak and propagate too fast (e.g. Hayashi and Sumi 1986; Hayashi and Golder 1986, 1988, Lau et al. 1988, Slingo et al. 1996; Waliser et al. 2003; Lin et al. 2006). The Atmospheric Model Intercomparison Project (AMIP) study by Slingo et al. (1996) found that no model has captured the dominance of the MJO in space-time spectral analysis found in observations, and nearly all have relatively more power at higher frequencies (<30 days) than in observations. Recently, Lin et al. (2006) evaluates the tropical intraseasonal variability in 14 coupled GCMs participating in the

1 Inter-governmental Panel on Climate Change (IPCC) Fourth Assessment Report (AR4).
2 The results show that current state-of-the-art GCMs still have significant problems and
3 display a wide range of skill in simulating the tropical intraseasonal variability. Most of
4 the models produce overly weak MJO variance and poor MJO propagation. Moreover,
5 the MJO variance in 13 of the 14 models does not come from a pronounced spectral peak,
6 but usually comes from part of an over-reddened spectrum, which in turn is associated
7 with too-strong persistence of equatorial precipitation.

8 Lin et al. (2006) also evaluated, for the first time in literature, other convectively
9 coupled equatorial waves simulated by the GCMs. About half of the models have signals
10 of convectively coupled equatorial waves, with Kelvin and MRG-EIG waves especially
11 prominent. However, the variances are generally too weak for all wave modes except the
12 $n=0$ EIG wave, and the phase speeds are generally too fast, suggesting that these models
13 may not have a large enough reduction in their “effective static stability” by diabatic
14 heating.

15 It is widely accepted that wave-heating feedback is central for the amplification and
16 maintenance of the convectively coupled equatorial waves. The total diabatic heating has
17 two main components: convective heating (release of latent heat, along with eddy flux
18 divergences that shape the profile) and radiative heating. Most theoretical studies have
19 focused only on the role of convective heating in wave-heating feedback. The
20 mechanisms studied include the wave-CISK (conditional instability of the second kind)
21 mechanism (e.g., Lau and Peng 1987), the frictional wave-CISK mechanism (e.g. Wang
22 and Rui 1990), the wind-induced surface heat exchange (WISHE) mechanism (e.g.,

Emanuel 1987; Neelin et al. 1987), and the charge–discharge mechanism (e.g., Blade and Hartmann 1993; Hayashi and Golder 1997).

The radiative heating, on the other hand, also contribute significantly to the total diabatic heating and thus may affect the convectively coupled equatorial waves. The radiative heating may be conveniently separated into two components: column-integrated heating and vertical heating profile, which have different effects on deep convection. The column-integrated heating tends to enhance the convective heating because in the convectively active phase of a convectively coupled equatorial wave, clouds and water vapor associated with deep convection reduce outgoing longwave radiation (OLR) to space and therefore increase radiative heating in the atmosphere. As a quantitative measure, *an enhancement factor of radiative heating can be defined as the ratio between the column-integrated radiative heating and the column-integrated convective heating.* Using collocated top-of-atmosphere (TOA) and surface radiative flux measurements from special field program data and long-term TOA flux data, Lin and Mapes (2004) examined the column-integrated radiation budget of the MJO, and found that the column-integrated radiative heating is nearly in phase with the precipitation and enhances the net condensation heating by about 10%–15%, with the dominant contribution from the reduction of OLR during wet periods. Recently, several modeling studies found that radiative heating can also significantly affect the amplitude and/or phase speed of the simulated intraseasonal oscillations (e.g. Raymond 2001; Sobel and Gildor 2003; Bony and Emanuel 2005). In an idealized model of thermodynamic atmosphere–ocean interaction on the intraseasonal time scale, Sobel and Gildor (2003) found that the enhancement factor of radiative heating is the most sensitive parameter, and both the

1 growth rate and the period of simulated intraseasonal oscillations increase with the
2 enhancement factor. In a theoretical model, Raymond (2001) demonstrated that when the
3 enhancement factor is very large the radiative heating can reduce the effective static
4 stability to a negative value, that is, to an effective static instability. He termed this
5 instability the radiative–convective instability. An MJO-like slow eastward-propagating
6 mode appears to develop in his model from this radiative–convective instability.

7 The second aspect of radiative heating is its vertical heating profile. Using the TOGA
8 COARE radiative heating profiles calculated by Qian (2003), Lin et al. (2004) analyzed
9 the vertical structure of radiative heating in the MJO. They found that during the
10 convectively active phase, radiative heating is characterized by warming in the lower and
11 middle troposphere but cooling in the upper troposphere. Such a heating profile tends to
12 suppress deep convection, in contrast to the enhancing effect of column-integrated
13 heating. Several previous GCM studies found that cloud radiative heating tends to
14 suppress the simulated MJO-like mode (e.g. Slingo and Madden 1991; Lee et al. 2001;
15 Lau et al. 2005). Lee et al. (2001) conducted two types of simulation: one with prescribed
16 zonal mean radiation and the other with fully interactive clouds and radiation. In contrast
17 to the fixed radiation case, where the MJO is simulated reasonably well, the cloud-
18 radiation interaction significantly contaminates the eastward propagation of the MJO by
19 producing small-scale disturbances moving westward with the easterly basic winds. The
20 small-scale disturbances are persistently excited by a strong positive feedback through
21 interaction between cumulus-anvil clouds and radiation. The longwave interaction is
22 shown to play a bigger role in contaminating the MJO than the shortwave interaction
23 does. The anvil clouds reduce the longwave cooling significantly in the lower

1 troposphere while releasing latent heating in the upper troposphere. To moderate the
2 strong cloud-radiation feedback, the large-scale condensation scheme in the GCM is
3 modified by reducing the autoconversion timescale, needed for cloud condensates to
4 grow up to rain drops. In addition, upper air ice cloud contents are reduced to change the
5 cloud albedo. These modifications make a more realistic simulation of the MJO similar to
6 the observed. However, the effects of cloud radiative heating on AGCM-simulated other
7 convectively coupled equatorial waves (e.g. Kelvin, n=1 ER, and MRG waves) have not
8 been studied.

9 The purpose of this study is to extend the Lee et al. (2001) study to examine the
10 effects of cloud radiative heating on AGCM-simulated convectively coupled equatorial
11 waves. Following Lee et al. (2001), the strength of cloud radiative heating is adjusted by
12 modifying the autoconversion timescale, needed for cloud condensates to grow up to rain
13 drops. The questions we address are: *Are the AGCM-simulated convectively coupled*
14 *equatorial waves sensitive to the strength of cloud radiative heating? Does cloud*
15 *radiative heating enhance or suppress the waves?*

16 The models and validation datasets used in this study are described in section 2. The
17 diagnostic methods are described in section 3. Results are presented in section 4. A
18 summary and discussion are given in section 5.

19

20 **2. Models and validation datasets**

21 The model used in this study is the Seoul National University atmospheric general
22 circulation model (SNUGCM). The model is a global spectral model, with 20 vertical
23 levels in a sigma coordinate. In this study, T42 ($\sim 2.8^\circ \times 2.8^\circ$) truncation is used for the

1 model horizontal resolution. Moist convection is represented by the simplified version of
2 the Relaxed Arakawa-Schubert (RAS) formulation (Numaguti et al. 1995). The large-
3 scale condensation scheme consists of a prognostic microphysics parameterization for
4 total cloud liquid water (Le Treut and Li, 1991) with a diagnostic cloud fraction
5 parameterization. Non-precipitating shallow convection scheme (Tiedtke 1983) is also
6 implemented in the model for the mid-tropospheric moist convection. The boundary
7 layer scheme is a non-local diffusion scheme based on Holtslag and Boville (1993), while
8 the land surface model is from Bonan (1996). The radiation process is parameterized by
9 the two-stream k distribution scheme implemented by Nakajima et al. (1995). Other
10 details of the model physics are described in Lee et al. (2001, 2003).

11 To examine the effects of cloud radiative heating on the simulated convectively
12 coupled equatorial waves, we tested the parameter sensitivity to the autoconversion
13 timescale in the large-scale condensation scheme. As discussed in Lee et al. (2001), this
14 parameter gives a characteristic time for auto-conversion of cloud droplets into
15 precipitating rain drops. As it becomes smaller, the precipitating process is faster with
16 shorter cloud lifetime, which can effectively reduce the magnitude of the cloud-radiative
17 heating (Lee et al. 2001). In this study, a wide range of autoconversion timescales were
18 tested for the timescale originally set to 9600 seconds, which are listed in Table 1. In
19 particular, we conducted a “no cloud” experiment (EXP0) in which all the condensates by
20 cumulus convection and large-scale condensation precipitate out instantaneously. In each
21 experiment, the minimum entrainment constraint in the RAS convection scheme was
22 commonly applied with a positive constant $\alpha=0.1$, which is same as in Lee et al. (2001).

Each run consists of 8 year AMIP-style simulations (1997-2004) driven by the same observed sea surface temperatures and sea-ice distributions.

The model simulations are validated using multiple observational datasets. To bracket the uncertainties associated with precipitation measurements/retrievals, especially the well-known difference between infrared (IR) based retrievals and microwave-based retrievals (e.g. Yuter and Houze 2000), we use two different precipitation datasets: (1) 8 years (1997-2004) of daily GOES Precipitation Index (GPI, Janowiak and Arkin 1991) precipitation with a horizontal resolution of 2.5 degree longitude by 2.5 latitude, which is retrieved based on IR measurements from multiple geostationary satellites; and (2) 8 years (1997-2004) of daily Global Precipitation Climatology Project (GPCP) One-Degree-Daily (1DD) Precipitation (Huffman et al. 2001) with a horizontal resolution of 1 degree longitude by 1 degree latitude. These are IR-based GPI retrievals scaled by the monthly means of microwave-based SSM/I retrievals.

3. Method

Through the space-time spectral analysis of outgoing longwave radiation (OLR), Takayabu (1994) and WK demonstrated that a significant portion of tropical cloudiness is organized in waves corresponding to the normal modes of the linear shallow water system isolated by Matsuno (1966). In WK, these spectra represent the power remaining in the symmetric and antisymmetric components of OLR about the equator after dividing raw wavenumber-frequency power spectra by an estimate of the background power spectrum. Peaks standing above the background correspond to the Kelvin, $n=1$ ER, MRG, $n=0$ EIG, $n=1$ WIG and $n=2$ WIG waves. It was found that the dispersion curves

1 that best match the wavenumber-frequency characteristics of these waves have
2 surprisingly shallow equivalent depths in the range of around 25 m, which is about an
3 order of magnitude smaller than that expected for a free wave with a similar vertical
4 wavelength twice the depth of the troposphere (e.g. Salby and Garcia 1987; Wheeler et
5 al. 2000).

6 Using the methodology of WK, space-time spectra of daily tropical precipitation were
7 obtained for the 8 years of model data used in this study and compared with those of
8 eight years of observed precipitation estimates from the GPI and 1DD data sets. We will
9 briefly outline this procedure here, and refer the reader to WK and Lin et al. (2006) for
10 further details.

11 The model and validation precipitation data were first interpolated to a zonal
12 resolution of 5 degrees longitude with the latitudinal resolution. We first decomposed the
13 precipitation into its antisymmetric and symmetric components, averaged these from 15N
14 to 15S, and computed spectra of the averaged values. To reduce noise the space-time
15 spectra were calculated as in WK for successive overlapping segments of data and then
16 averaged, here 128 days long with 78 days of overlap between each segment. Complex
17 Fourier coefficients are first obtained in zonal planetary wavenumber space, which are
18 then subjected to a further complex FFT to obtain the wavenumber-frequency spectrum
19 for the symmetric and antisymmetric components of precipitation about the equator.

20 An estimate of the "background" space-time spectrum is obtained for each data set by
21 averaging the power of the symmetric and antisymmetric spectra and smoothing this by
22 successive passes of a 1-2-1 filter in frequency and wavenumber (see WK). The raw
23 spectra are then divided by this background to obtain an estimate of the signal standing

1 above the background noise. Here we assume the signal is significant if it stands at 1.2
2 times (or 20% above) the background. It should be emphasized that, while this is only a
3 rough estimate of the true "significance" of the signals, the intent is to simply identify
4 those modes which might represent signals in rainfall standing above a simple red noise
5 continuum that would presumably prevail if rainfall were not organized by disturbances
6 on the large scale.

7 The definitions of Kelvin, $n=1$ ER, MRG, $n=0$ EIG and $n=1$ WIG modes are as in
8 WK and Lin et al. (2006). Each mode was isolated by filtering in the wavenumber-
9 frequency domain (see Fig. 6 of WK for the defined regions of filtering for each wave),
10 and the corresponding time series were obtained by an inverse space-time Fourier
11 transform.

12 As in Lin et al. (2006) the MJO is defined as significant rainfall variability in
13 eastward wavenumber 1-6 and in the period range of 30-70 days. The variance of the
14 MJO anomaly was also compared with the variance of its westward counterpart, i.e., the
15 westward wavenumbers 1 through 6, 30-70 day anomaly, which was isolated using the
16 same method as above.

17 It is important to note that the diabatic heating processes are generally nonlinear, and
18 the equatorial wave mode decomposition approach is an approximation of the
19 convectively coupled modes based on the concept of the free modes with proper
20 adjustment of the equivalent depth. Nonlinear dynamical processes also play a significant
21 role in the organization, so that the heating associated with one particular mode (as
22 isolated by the above linear decomposition method) is determined not only by the mode
23 itself, but also by the time-mean field and the rectification effects of subscale modes.

4. Results

a Climatological precipitation in the equatorial belt

Previous observational studies indicate that the intraseasonal variance of convection is highly correlated with time-mean convective intensity (e.g. WK, Hendon et al. 1999). Therefore we first look at the eight-year time-mean precipitation along the equatorial belt, especially over the Indo-Pacific warm pool region, where most of the convectively coupled equatorial waves have the largest variance (WK). Figure 1 shows the annual mean precipitation versus longitude averaged between (a) 15N and 15S, and (b) 5N and 5S. To focus on the large-scale features, we smoothed the data zonally to retain only zonal wavenumbers 0 through 6. Figure 1 demonstrates two points. First, all experiments simulate reasonably the basic feature of observed precipitation, with the primary maximum over the Indo-Pacific warm pool region, and a secondary local maximum over Central/South America. Within the warm pool region, all experiments also reproduce the local minimum of precipitation over the maritime continent, but there is a positive bias over the western Pacific and a negative bias over the eastern Indian Ocean. Outside the warm pool region, all experiments produce quite realistic magnitude of precipitation over Central/South America. Comparing with the 15N-15S average (Figure 1a), the biases in 5N-5S average (Figure 1b) are smaller over western Pacific, but larger over eastern Indian Ocean. Second, changing the autoconversion rate does not change much the mean precipitation over the Indo-Pacific warm pool region, and thus any difference in the intraseasonal variability in this region is likely due to change in cloud-radiation feedback instead of change in mean precipitation. Outside the warm pool region, increasing the

1 autoconversion rate significantly increases mean precipitation over the continents of
2 Africa and South America.

3 Although changing the autoconversion rate does not change much the time-mean
4 precipitation over the Indo-Pacific warm pool region, it significantly changes the time-
5 mean clouds, radiative heating and vertical structure of the tropical atmosphere. As an
6 example, Figure 2 shows the longitude-height cross section of EXP2-EXP7 difference in
7 annual mean (a) cloud amount, (b) longwave heating rate, (c) shortwave heating rate, and
8 (d) total radiative heating rate averaged between 20N-20S. Increasing autoconversion rate
9 substantially reduces the annual mean cloud amount in the upper troposphere and to a
10 lesser extent in the lower troposphere near the surface (Figure 2a). The decrease in cloud
11 amount leads to reduction in longwave heating rate near the cloud base, but increase in
12 longwave heating rate at the cloud top (Figure 2b). It also leads to decrease of shortwave
13 heating rate in the upper part of the clouds (Figure 2c), which largely cancels the increase
14 of longwave heating there. Therefore, the total radiative heating decreases both in the
15 upper troposphere and near the surface (Figure 2d).

16 The changes in autoconversion rate and radiative heating also lead to changes in
17 moist processes and associated heating (Figure 3). The heating due to convection (Figure
18 3a) increases in the upper troposphere between 300-600 mb, but decreases near the
19 tropopause. On the other hand, the heating due to large-scale condensation (Figure 3b)
20 often shows sign opposite to that due to deep convection, with decrease in the upper
21 troposphere between 250-500 mb but increase both near the tropopause and in the lower
22 troposphere. When they are added together, the total heating due to moist processes
23 slightly increases throughout the troposphere in many regions (Figure 3c), which is not

1 large enough to compensate the decrease of radiative heating in the warm pool region
2 (Figure 2d). Therefore, the total diabatic heating decreases in the upper troposphere in
3 the warm pool region (Figure 3d).

4 The change in diabatic heating leads to change in temperature (Figure 4a), which is
5 characterized by a significant cooling in the upper troposphere. The temperature change
6 is more spatially homogeneous than other fields, which may be caused by the very weak
7 Coriolis force near the equator, leading to very weak pressure gradient and temperature
8 gradient. This is often referred to as the “weak temperature gradient” hypothesis in
9 theoretical models (e.g. Sobel and Bretherton 2000, Bretherton and Sobel 2002, Majda
10 and Klein 2003). Consistent with enhancement of convection (Figure 3a) and large-scale
11 condensation (Figure 3b), the humidity change (Figure 4b) is characterized by significant
12 drying in the lower troposphere.

13 The above results shown in Figure 2-Figure 4 are for the differences between EXP2
14 and EXP7 (control run). Other experiments with autoconversion rate higher than EXP7
15 generally show pattern of differences similar to EXP7, while the EXP8 experiment,
16 which has an autoconversion rate lower than EXP7, shows the opposite sign of
17 differences (not shown). The whole picture is quite consistent with the results of Lau et
18 al. (2005), with our EXP2 similar to their E1 experiment and our EXP7 similar to their
19 E2 experiment. Lau et al. (2005) did a detailed analysis of the microphysical mechanism
20 for the changes in mean state, and found that a faster autoconversion rate leads to more
21 warm rain, which produces more condensational heating in the lower troposphere. The
22 vertical differential heating between condensational heating in the lower troposphere and
23 radiative cooling in the upper troposphere destabilizes the tropical atmosphere, producing

1 a positive feedback via secondary circulation between convective tower and anvil regions
2 (cold rain), and adjacent middle-to-low cloud (warm rain) regions. Because the focus of
3 the present study is on tropical intraseasonal variability rather than the mean state, we
4 will not repeat the analysis of Lau et al. (2005) but refer the interested reader to their
5 paper for more detailed analysis of the underlying microphysical mechanism.

6 To summarize, the climatological precipitation over the Indo-Pacific warm pool is
7 reasonably simulated by all experiments. Changing the autoconversion rate has little
8 effect on the climatological mean precipitation, suggesting that any related change in
9 intraseasonal variability is likely due to change in cloud-radiation feedback instead of
10 change in mean precipitation. Nevertheless, increasing autoconversion rate significantly
11 reduces the time-mean clouds and radiative heating both in the upper troposphere and
12 near the surface, and enhances heating due to moist processes in the middle troposphere.
13 These lead to cooling of time-mean upper troposphere temperature and drying of lower
14 troposphere moisture. As will be shown in section 4d, the changes in time-mean
15 thermodynamical structure affect the wave-heating feedback in the convectively coupled
16 equatorial waves.

17 18 *b Total intraseasonal (2-128 day) variance*

19 Figure 5 shows the total variance of the 2-128 day filtered precipitation anomaly
20 along the equator averaged between 15N-15S. There are two important things to note
21 concerning Figure 5. First, the total intraseasonal variance in most experiments is overly
22 large over western Pacific, although it is overly small over Indian Ocean. This is very
23 encouraging because 13 of the 14 IPCC AR4 GCMs analyzed by Lin et al. (2006)

1 produce overly small variance over both western Pacific and Indian Ocean, although their
2 annual mean precipitation is often as large as in the SNU model studied here. Second,
3 increasing the autoconversion rate (i.e. reducing cloud-radiative heating) tends to enhance
4 the total intraseasonal variance over western Pacific, Indian Ocean, South America and
5 Africa. The enhancement is not always monotonic. For example, EXP0 (the “no cloud”
6 experiment) produces less variance than most of the other experiments over western
7 Pacific.

9 *c Dominant intraseasonal modes*

10 Figure 6 and Figure 7 show the results of dividing the symmetric and antisymmetric
11 raw spectra by the estimates of their background spectra. This normalization procedure
12 removes a large portion of the systematic biases within the various models and observed
13 data sets, more clearly displaying the model disturbances with respect to their own
14 climatological variance at each scale. Signals of the Kelvin, $n=1$ ER, and $n=1$ WIG waves
15 are readily identified in the observational symmetric spectra (Figure 6a), along with the
16 MRG and $n=0$ EIG waves in the antisymmetric spectra (Figure 7a). Dispersion curves of
17 the shallow water modes are also shown on all spectra, corresponding to equivalent
18 depths of 12, 25, and 50 m. As in the OLR spectra of WK, all of the observed spectral
19 peaks corresponding to shallow water modes best match an equivalent depth of around 25
20 m in the observational rainfall data.

21 The model spectra in Figure 6 and Figure 7 demonstrate three points. First, many
22 experiments produce pronounced signals of convectively coupled equatorial waves, with
23 Kelvin and MRG-EIG waves especially prominent. The phase speed is quite realistic for

1 all the wave modes except the $n=0$ EIG wave which displays a too-fast phase speed.
2 These support our use of the SNUGCM to examine the effect of cloud-radiation feedback
3 on the waves. Second, increasing the autoconversion rate significantly enhances the
4 prominence of the Kelvin and $n=0$ EIG waves. Third, changing the autoconversion rate
5 has little effect on the phase speed of the waves.

6 When a model displays signals of a certain wave mode in Figure 6 and Figure 7, it
7 means that the variance of that wave mode stands out above the background spectra (i.e.,
8 a high signal-to-noise ratio), but the absolute value of the variance of that wave mode
9 may not be large. Therefore, it is of interest to look further at the absolute values of the
10 variance of each wave mode. Figure 8 shows the variances of the (a) MJO, (b) Kelvin, (c)
11 $n=1$ ER, (d) MRG, (e) $n=0$ EIG, and (f) $n=1$ WIG modes along the equator averaged
12 between 15N and 15S. Figure 8 demonstrates four points. First, increasing the
13 autoconversion rate tends to enhance significantly the variance of the Kelvin wave
14 (Figure 8b), ER wave (Figure 8c), MRG wave (Figure 8d) and $n=1$ WIG wave (Figure
15 8f), and the model variance for very fast autoconversion rate sometimes approaches the
16 observed variance. This is encouraging because among the 14 IPCC AR4 GCMs
17 analyzed by Lin et al. (2006), only a couple of models produce wave variances
18 approaching the observed values. Second, the increase of variance for the above waves is
19 not always monotonic with increasing autoconversion rate. In particular, EXP0 (the “no
20 cloud” experiment) often produces weaker variance than EXP1 and EXP2. This is
21 probably due to some nonlinear processes associated with cloud microphysics, radiation
22 or convection. Third, changing autoconversion rate does not change much the variance of
23 the MJO (Figure 8a), which is always much smaller than the observed value. This further

1 illustrate that MJO, as a combined Kelvin-Rossby mode (e.g. Salby and Hendon 1994),
2 has quite different dynamics from the Kelvin mode. Fourth, changing autoconversion
3 rate does not affect systematically the variance of $n=0$ EIG wave (Figure 8e), which is
4 larger than the observed value in most of the experiments. This is consistent with the
5 finding of Lin et al. (2006) that most of the IPCC AR4 models can produce large variance
6 for $n=0$ EIG wave although they produce very weak variance for other waves. In other
7 words, the variance of $n=0$ EIG wave seems to be independent of model physics, which is
8 very interesting and needs further studies in the future.

9 In summary, all experiments produce prominent signals of convectively coupled
10 equatorial waves, with Kelvin and MRG-EIG waves especially prominent and the phase
11 speeds generally quite realistic. These support our use of the SNUGCM to examine the
12 effect of cloud-radiation feedback on the convectively coupled equatorial waves.
13 Increasing autoconversion rate enhances the prominence of Kelvin and $n=0$ EIG waves. It
14 also tend to enhance significantly the variance of the Kelvin, ER, MRG and $n=1$ WIG
15 waves, but not the MJO or $n=0$ EIG wave. Changing autoconversion rate has little effect
16 on the phase speed of the waves.

17 *d Vertical structure of diabatic heating and wave-heating feedback*

19 To further understand the effects of changing autoconversion rate on simulations of
20 convectively coupled equatorial waves, we first analyze in this subsection the vertical
21 structure of diabatic heating at the intraseasonal timescale, including both the radiative
22 heating and heating due to moist processes. Figure 9 shows the linear regression against
23 *daily* surface precipitation for the vertical profiles of (a) cloud amount, (b) shortwave

1 heating rate, (c) longwave heating rate, and (d) total radiative heating rate. Increasing
2 autoconversion rate significantly reduces the cloud amount in the upper and middle
3 troposphere, but slightly increases the cloud amount in the lower troposphere (Figure 9a).
4 The reduction of clouds between 200-800 mb leads to weakening of longwave cloud-top
5 cooling and cloud-base warming (Figure 9b), as well as shortwave in-cloud warming and
6 below-cloud cooling (Figure 9c). Therefore, the total radiative heating is significantly
7 reduced between 250mb and 950mb, but is slightly increased above 250 mb, and remain
8 almost unchanged near the surface (Figure 9d). The vertically integrated radiative heating
9 per unit precipitation, which is the enhancement factor discussed in the introduction, is
10 thus decreased.

11 The reduction of radiative heating in most of the free troposphere, together with the
12 almost unchanged radiative heating near the surface, tends to increase the convective
13 instability. Indeed, the deep convection penetrates to a higher altitude (Figure 10a).
14 However, reduction of upper level clouds leads to significant weakening of the large-
15 scale condensation process and associated upper-tropospheric warming/lower-
16 tropospheric cooling (Figure 10b). Therefore, the vertical profile of total heating due to
17 moist processes becomes less top-heavy with increasing autoconversion rate (Figure
18 10c). The total diabatic heating (radiative heating plus heating due to moist processes),
19 usually referred to as Q_1 , just becomes smaller per unit precipitation but with no
20 significant change in its top-heaviness (Figure 10d).

21 How do the changes in diabatic heating structure affect the convectively coupled
22 equatorial waves? As discussed in the introduction, most of the theories of convectively
23 coupled equatorial waves emphasize the role of wave-heating feedback in determining

1 the phase speed and amplitude of the waves (e.g. Lau and Peng 1987; Emanuel 1987;
 2 Neelin et al. 1987; Wang and Rui 1990; Blade and Hartmann 1993; Hayashi and Golder
 3 1997; Raymond 2001). For dry waves, the phase speed is generally determined by the dry
 4 static stability. For the moist waves, on the other hand, the phase speed is generally
 5 determined by the effective static stability (e.g. Raymond 2001), with higher effective
 6 static stability generally associated with faster wave speeds. Following Raymond (2001)
 7 and Lin et al. (2002), the effective static stability is defined as:

$$8 \quad \Gamma_{eff}(p) = \frac{\partial \theta}{\partial p} - \frac{\partial S_{\theta}}{\partial \omega} \quad (1)$$

9 where θ is the potential temperature. S_{θ} is the potential temperature source produced by
 10 the diabatic parameterizations, and ω is the vertical pressure velocity. $\partial \theta / \partial p$ is the dry
 11 static stability. $\partial S_{\theta} / \partial \omega$ represents the effect of diabatic heating, and its value is estimated
 12 as follows: At each level we fit a straight line to a scatterplot of S_{θ} versus ω for all grid
 13 points in a specified subdomain of the numerical solution. The slope of this line is taken
 14 as the estimate of $\partial S_{\theta} / \partial \omega$.

15 The calculated results are shown in Figure 11. The effective static stability does not
 16 change much with change in autoconversion rate (Figure 11a). *This explains the nearly*
 17 *unchanged phase speeds of the waves with respect to different autoconversion rates*
 18 (Figure 6 and Figure 7). Actually, the dry static stability decreases significantly in the
 19 upper troposphere with increasing autoconversion rate (Figure 11b), which is caused by
 20 significant cooling of time-mean temperature in the upper troposphere (Figure 4a).
 21 However, the reduction of total diabatic heating associated with vertical motion (Figure
 22 11c), which is consistent with the reduction of diabatic heating per unit precipitation

(Figure 10d), almost cancels the reduction of dry static stability, leading to the nearly constant effective static stability.

The changes of prominence and variance of the waves (Figure 6, Figure 7 and Figure 8) are more difficult to understand because (1) the variance increases with increasing autoconversion rate only for some of the waves but not others, and (2) until now there is no satisfying theory on what determines the wave variances in GCMs. Most of the theoretical studies on convectively coupled equatorial waves focus on the Kelvin wave. Therefore we plot in Figure 12 the composite life cycle of Kelvin wave in both EXP7 (control run) and EXP2. All data are area-averaged over 5N-5S, 150-160E. The composite life cycle is constructed using lag-regression of each variable against the Kelvin wave precipitation anomaly. The lag-0 regressions of the different heating terms are similar to those shown in Figure 9 and Figure 10, and thus will not be discussed here. We will focus on the developing stage of the Kelvin wave around lag -3 days. Increasing autoconversion rate significantly reduces the cloud amount in the upper troposphere at the developing stage (Figure 12a, b). This leads to an enhancement of longwave heating in the boundary layer (Figure 12c, d), and slight enhancement of shortwave heating in the middle troposphere (Figure 12e, f). The total radiative heating thus increases near the surface at the developing stage (Figure 12g, h). Although the heating due to moist processes does not change much in the boundary layer (Figure 12i, j), the total diabatic heating does increase in the boundary layer (Figure 12k, l), which is associated with increase of vertical motion in the boundary layer (Figure 12m, n) implying an enhancement of boundary layer convergence. This will enhance the frictional wave-CISK feedback mechanism and increase the wave variance (e.g. Wang and Rui 1990).

1 We do not find evidence for the enhancement of other feedback mechanisms in the
2 Kelvin wave. For example, in the free-troposphere wave-CISK mechanism (e.g. Lau and
3 Peng 1987), wave growth rate is determined by three factors: (1) time-mean low-level
4 moisture with higher moisture leading to larger amplitude, (2) phase tilt of heating with
5 height with larger tilt leading to larger amplitude, and (3) vertical heating profile with
6 contradicting results from different studies (e.g. Lau and Peng 1987; Chang and Lim
7 1988; Cho and Pendlebury 1997). As shown in Figure 4b, the time-mean low-level
8 moisture decreases with increasing autoconversion rate, which tends to suppress rather
9 than amplify the wave variance. We do not see any significant difference between EXP2
10 and EXP7 in phase tilt in the free troposphere or vertical heating profile (Figure 12k, l).
11 Therefore, it seems that free-troposphere wave-CISK mechanism does not contribute to
12 the enhancement of Kelvin wave variance.

13 Figure 13 is same as Figure 12 but for the MJO. Similar to the Kelvin wave,
14 increasing autoconversion rate also decreases cloud amount in the upper troposphere in
15 the MJO at the developing stage around lag -10 days (Figure 13a, b), which leads to
16 enhancement of longwave heating in the boundary layer (Figure 13c, d) and enhancement
17 of total radiative heating in the boundary layer (Figure 13g, h). However, for some
18 unknown reason, heating due to moist processes reduces in the boundary layer at the
19 developing stage (Figure 13i, j), which is in contrast with the Kelvin wave (Figure 12i, j).
20 This cooling cancels the warming due to radiative heating, making the total diabatic
21 heating nearly unchanged in the boundary layer at the developing stage (Figure 13k, l).
22 Therefore the vertical velocity and associated boundary layer convergence are nearly
23 unchanged, and the frictional wave-CISK feedback is not enhanced. Total diabatic

1 heatings in EXP7 and EXP2 also have similar phase tilt in the free troposphere and
2 similar vertical heating profile (Figure 13k, l). The quite similar MJO heating structures
3 in EXP7 and EXP2 may explain partly the unchanged MJO variance associated with
4 changing autoconversion rate.

5 Observations are showing the importance of life cycles of convective processes,
6 including moisture recycling from shallow convection, deep convection and stratiform
7 precipitation, in leading to large-scale organization of convection (e.g. Lin et al. 2004;
8 Mapes et al. 2006). The insensitivity of the MJO variance to cloud-radiative processes
9 found here might be model dependent due to the inadequacy of representation of
10 moisture recycling processes by shallow convection in this model as in many other GCMs.
11 The standard setup of the RAS convection scheme used in our experiments favors the
12 development of deep convection over shallow convection. Lin et al. (2007) added a
13 moisture trigger to the RAS scheme to encourage the development of shallow/midtop
14 convection when the lower troposphere is dry, and found that the MJO propagation is
15 improved. Therefore, it is important to parameterize well the life cycle of convective
16 processes, especially the shallow convection in the early stage, in order to simulate well
17 the MJO. Much more analyses are needed in future studies to understand the physical
18 mechanisms for other waves (ER, MRG, EIG and WIG).

20 **5. Summary and discussion**

21 This study examines the effects of cloud-radiative heating on convectively coupled
22 equatorial waves simulated by the SNUGCM. The strength of cloud-radiative heating is
23 adjusted by modifying the autoconversion rate needed for cloud condensates to grow up

1 to rain drops. The results show that increasing the autoconversion rate has little effect on
2 the climatological mean precipitation, but it significantly reduces the time-mean clouds
3 and radiative heating in the upper troposphere and enhances heating due to moist
4 processes in the middle troposphere. These lead to cooling of time-mean upper
5 troposphere temperature and drying of lower troposphere moisture. Reduction of cloud-
6 radiative heating enhances the prominence of Kelvin and $n=0$ EIG waves. It also tend to
7 enhance significantly the variance of the Kelvin, ER, MRG and $n=1$ WIG waves, but not
8 the MJO or $n=0$ EIG wave. Reduction of cloud-radiative heating has little effect on the
9 phase speed of the waves, which is associated with unchanged effective static stability
10 caused by the near cancellation between reduced dry static stability and reduced diabatic
11 heating.

12 The main finding of this study is that cloud-radiative heating tends to suppress
13 AGCM-simulated convectively coupled equatorial waves. As discussed in the
14 introduction, the cloud-radiative heating has two aspects which have opposite effect on
15 convective heating: the column-integrated cloud-radiative heating enhances the
16 convective heating, but the vertical profile of cloud-radiative heating tends to suppress
17 deep convection and convective heating. Therefore, modeling studies are needed to
18 determine the sign of the net effect. Most of the theoretical modeling studies mainly
19 considered the first effect, i.e., the enhancing effect of column-integrated heating (e.g.
20 Raymond 2001; Sobel and Gildor 2003; Bony and Emanuel 2005). The GCM
21 experiments, on the other hand, consider both the enhancing effect of column-integrated
22 heating and the suppressing effects of vertical radiative heating profile. The radiative
23 heating profiles in our model experiments have been analyzed by Lee et al. (2001) and

1 are quite similar to those derived from observational data (e.g. Qian 2003). Our results
2 show that the net effect of radiative heating is suppressing most of the convectively
3 coupled equatorial waves, suggesting that the effect of vertical heating profile dominates
4 over that of the column-integrated heating.

5 Our results have important implications for improving GCM simulations of
6 convectively coupled equatorial waves and MJO. The cloud-radiative fluxes and heating
7 in GCMs are often tuned to match the observed TOA and surface fluxes, and our results
8 suggest that such tuning may have strong effects on the simulated convectively coupled
9 equatorial waves. For example, Figure 14a shows the annual mean OLR along the
10 equator averaged between 5N-5S for observation and the different model experiments.
11 The experiments that fit best the observation are EXP6, EXP7 and EXP8. However, when
12 considering the linear regression of $-OLR$ versus precipitation (Figure 14b), which is a
13 good estimate of the enhancement factor of cloud-radiative heating discussed in the
14 introduction, EXP4 fits best with the observation. In other words, although EXP6, EXP7
15 and EXP8 simulate better time-mean TOA longwave flux, they overestimate the cloud-
16 radiative heating at the intraseasonal time-scale, and thus suppress many convectively
17 coupled equatorial waves. Therefore, caution should be taken when tuning the TOA
18 radiative fluxes, and it would be better to check simultaneously the enhancement factor of
19 cloud-radiative heating at the intraseasonal time-scale. Actually this additional constraint
20 may help the model to get a more realistic distribution of different cloud types (e.g.
21 Hartmann et al. 2001).

1 **Acknowledgements**

2 We would like to thank the two anonymous reviewers for their insightful reviews of
3 the manuscript. J. L. Lin was supported by the NOAA CPO/CVP Program, NOAA
4 CPO/CDEP Program, and NASA MAP Program. I.-S. Kang was supported by the Korea
5 Meteorological Administration Research and Development Program under Grant
6 CATER_2007-4206 and BK21 program.

REFERENCES

- Bergman, J. W., H. H. Hendon, K. M. Weickmann, 2001: Intraseasonal Air-Sea Interactions at the Onset of El Nino. *J. Climate*, **14**, 1702-1719.
- Bessafi, M. and M.C. Wheeler, 2005: Modulation of south Indian Ocean tropical cyclones by the Madden-Julian oscillation and convectively-coupled equatorial waves. *Mon. Wea. Rev.*, 134, 638-656.
- Bladé I., and D. L. Hartmann, 1993: Tropical intraseasonal oscillations in a simple nonlinear model. *J. Atmos. Sci.*, **50**, 2922–2939.
- Bonan, G. B., A land surface model (LSM version 1.0) for ecological, hydrological, and atmospheric studies: Technical description and user's guide. NCAR *Tech. Note NCAR/TN-417+STR*, Natl. Cent. For Atmos. Res., 150pp., Boulder, Colorado.
- Bony, S., and Kerry A. Emanuel, 2005: On the Role of Moist Processes in Tropical Intraseasonal Variability: Cloud–Radiation and Moisture–Convection Feedbacks. *J. Atmos. Sci.*, 62, 2770-2789.
- Bretherton, C. S., and A. H. Sobel, 2002: A simple model of a convectively coupled Walker circulation using the weak temperature gradient approximation. *J. Climate.*, **15**, 2907–2920.
- Chang C. P., and H. Lim, 1988: Kelvin wave–CISK: A possible mechanism for the 30–50 day oscillations. *J. Atmos. Sci.*, **45**, 1709–1720.
- Cho H.-R., and D. Pendlebury, 1997: Wave CISK of equatorial waves and the vertical distribution of cumulus heating. *J. Atmos. Sci.*, **54**, 2429–2440.
- Dickinson, M., and Molinari J., 2002: Mixed Rossby–gravity waves and western Pacific tropical cyclogenesis. Part I: Synoptic evolution. *J. Atmos. Sci.*, **59**, 2183–2196.

- Duchan, C.E., 1979: Lanczos filtering in one and two dimensions. *J. Appl. Meteor.*, **18**, 1016-1022.
- Emanuel K. A., 1987: An air-sea interaction model of intraseasonal oscillation in the Tropics. *J. Atmos. Sci.*, **44**, 2324-2340.
- Emanuel, K. A., J. D. Neelin, and C. S. Bretherton, 1994: On large-scale circulations in convecting atmospheres. *Quart. J. Roy. Meteor. Soc.*, **120**, 1111-1143.
- Haertel, P. T., and G. N. Kiladis, 2004: On the dynamics of two-day equatorial disturbances. *J. Atmos. Sci.*, submitted.
- Hartmann, D. L., L. A. Moy, and Q. Fu, 2001: Tropical Convection and the Energy Balance at the Top of the Atmosphere. *J. Climate*, **14**, 4495-4511.
- Hayashi, Y., and A. Sumi, 1986: The 30-40 day oscillation simulated in an "aqua planet" model. *J. Meteor. Soc. Japan.*, **64**, 451-466.
- Hayashi, Y., and D. G. Golder, 1986: Tropical intraseasonal oscillations appearing in a GFDL general circulation model and FGGE data. Part I: Phase propagation. *J. Atmos. Sci.*, **43**, 3058-3067.
- Hayashi, Y., and D. G. Golder, 1988: Tropical intraseasonal oscillations appearing in a GFDL general circulation model and FGGE data. Part II: Structure. *J. Atmos. Sci.*, **45**, 3017-3033.
- Hendon, H.H., C. Zhang, and J.D. Glick, 1999: Interannual variation of the MJO during austral summer. *J. Climate*, **12**, 2538-2550.
- Holtstag, A. A. M., and B. A. Boville, 1993: Local versus nonlocal boundary layer diffusion in a global climate model. *J. Clim.*, **6**, 1825-1642.

- Huffman, G.J., R.F. Adler, M.M. Morrissey, S. Curtis, R. Joyce, B. McGavock, and J. Susskind, 2001: Global precipitation at one-degree daily resolution from multi-satellite observations. *J. Hydrometeor.*, **2**, 36-50.
- Janowiak, J. E., and P. A. Arkin, 1991: Rainfall variations in the Tropics during 1986-1989, as estimated from observations of cloud-top temperatures. *J. Geophys. Res.*, **96** (Suppl.), 3359-3373.
- Kessler, W. S., and M. J. McPhaden, and K. M. Weickmann, 1995: Forcing of intraseasonal Kelvin waves in the equatorial Pacific. *J. Geophys. Res.*, **100**, 10613-10631.
- Knutson, T. R., and K. M. Weickmann, 1987: 30–60 Day Atmospheric Oscillations: Composite Life Cycles of Convection and Circulation Anomalies. *Monthly Weather Review*, **115**, 1407–1436.
- Knutson, T. R., Klaus M. Weickmann and John E. Kutzbach. 1986: Global-Scale Intraseasonal Oscillations of Outgoing Longwave Radiation and 250 mb Zonal Wind during Northern Hemisphere Summer. *Monthly Weather Review*, **114**, 605–623.
- Lau, K. M., and P. H. Chan, 1985: Aspects of the 40-50-day oscillation during the northern winter as inferred from outgoing longwave radiation. *Mon. Wea. Rev.*, **113**, 1889-1909.
- Lau K. M., and L. Peng, 1987: Origin of low-frequency (intraseasonal) oscillations in the tropical atmosphere. *J. Atmos. Sci.*, **44**, 950–972.
- Lau, K. M., H. T. Wu, Y. C. Sud, and G. K. Walker, 2005: Effects of Cloud Microphysics on Tropical Atmospheric Hydrologic Processes and Intraseasonal Variability. *J. Climate*, **18**, 4731-4751.

- Lau, N. C., I. M. Held, and J. D. Neelin, 1988: The Madden-Julian oscillations in an idealized general circulation model. *J. Atmos. Sci.*, **45**, 3810-3831.
- Lee, M.-I., I.-S. Kang, J.-K. Kim, and B. E. Mapes, 2001: Influence of cloud-radiation interaction on simulating tropical intraseasonal oscillation with an atmospheric general circulation model, *J. Geophys. Res.*, **106**, 14219-14233.
- Lee, M.-I., I.-S. Kang, and B.E. Mapes, 2003: Impacts of cumulus convection parameterization on aqua-planet AGCM simulations of tropical intraseasonal variability. *J. Meteor. Soc. Japan*, **81**, 963-992.
- Le Treut, H., and Z. -X. Li, 1991: Sensitivity of an atmospheric general circulation model to prescribed SST changes: feedback effects associated with the simulation of cloud optical properties. *Clim. Dyn.*, **5**, 175-187.
- Liebmann, B., H. H. Hendon, and J. D. Glick, 1994: The relationship between tropical cyclones of the western Pacific and Indian Oceans and the Madden-Julian oscillation. *J. Meteor. Soc. Japan*, **72**, 401-411.
- Liebmann, B., and C. A. Smith, 1996: Description of a complete (interpolated) outgoing longwave radiation dataset. *Bull. Amer. Meteor. Soc.*, **77**, 1275-1277.
- Lin, J. L., 2006: The double-ITCZ problem in IPCC AR4 coupled GCMs: Ocean-atmosphere feedback analysis. *J. Climate*, in press. Pdf file available at <http://www.cdc.noaa.gov/people/jialin.lin/>
- Lin, J. L., and B. E. Mapes, 2004: Radiation budget of the tropical intraseasonal oscillation. *J. Atmos. Sci.*, **61**, 2050-2062.

- Lin, J. L., B. E. Mapes, M. H. Zhang and M. Newman, 2004: Stratiform precipitation, vertical heating profiles, and the Madden-Julian Oscillation. *J. Atmos. Sci.*, **61**, 296-309.
- Lin, J. L., M. H. Zhang, and B. E. Mapes, 2002: Does the tropical atmosphere support large-scale radiative-convective overturning? Proc. 25th Conference on Hurricanes and Tropical Meteorology, Amer. Met. Soc., 29 April-3 May 1997, San Diego, CA, 589-590.
- Lin, J. L., M. H. Zhang, and B. E. Mapes, 2005: Zonal momentum budget of the Madden-Julian Oscillation: The sources and strength of equivalent linear damping. *J. Atmos. Sci.*, **62**, 2172-2188.
- Lin, J. L., G.N. Kiladis, B.E. Mapes, K.M. Weickmann, K.R. Sperber, W.Y. Lin, M. Wheeler, S.D. Schubert, A. Del Genio, L.J. Donner, S. Emori, J.-F. Guérémy, F. Hourdin, P.J. Rasch, E. Roeckner, and J.F. Scinocca, 2006: Tropical intraseasonal variability in 14 IPCC AR4 climate models. Part I: Convective signals. *J. Climate*, **19**, 2665-2690.
- Lin, J. L., M.-I. Lee, D. Kim, I.-S. Kang, and Dargan Frierson, 2007: The impacts of convective parameterization and moisture triggering on AGCM-simulated convectively coupled equatorial waves. *J. Climate*, in press.
- Madden, R. A., and P. R. Julian, 1971: Detection of a 40-50 day oscillation in the zonal wind in the tropical Pacific. *J. Atmos. Sci.*, **28**, 702-708.
- Madden, R. A., and P. R. Julian, 1972: Description of global-scale circulation cells in the tropics with a 40-50 day period. *J. Atmos. Sci.*, **29**, 1109-1123.

- Madden, R. A., and P. R. Julian, 1994: Observations of the 40-50-day tropical oscillation-A review. *Mon. Wea. Rev.*, **122**, 814-837.
- Majda, A. J., and R. Klein, 2003: Systematic multiscale models for the Tropics. *J. Atmos. Sci.*, **60**, 393-408.
- Maloney, E. D., and D. L. Hartmann, 2000: Modulation of eastern North Pacific hurricanes by the Madden-Julian oscillation. *J. Climate.*, **13**, 1451-1460.
- Maloney, E. D., Hartmann, D. L. 2001: The Madden-Julian Oscillation, Barotropic Dynamics, and North Pacific Tropical Cyclone Formation. Part I: Observations. *J. Atmos. Sci.*, **58**, 2545-2558.
- Mapes, B. E., and R. A. Houze, 1995: Diabatic divergence profiles in western Pacific mesoscale convective systems. *J. Atmos. Sci.*, **52**, 1807-1828.
- Mapes, B. E., and J. L. Lin, 2005: Doppler radar observations of mesoscale wind divergence in regions of tropical convection. *Mon. Wea. Rev.*, **133**, 1808-1824.
- Mapes, B.E., S. Tulich, J. L. Lin, and P. Zuidema, 2006: Mesoscale convection life cycle: Building block or prototype for large-scale tropical waves? *Dyn. Atmos. Oceans*, **42**, 3-29.
- Moorthi, S., and Suarez M. J., 1992: Relaxed Arakawa-Schubert: A parameterization of moist convection for general circulation models. *Mon. Wea. Rev.*, **120**, 978-1002.
- Murakami, M., 1979: Large-scale aspects of deep convective activity over the GATE area. *Mon. Wea. Rev.*, **107**, 994-1013.
- Nakajima, T., M. Tsukamoto, Y. Tsushima, and A. Numaguti, 1995: Modelling of the radiative processes in an AGCM, in *Climate System Dynamics and Modelling*, vol. I-3, edited by T. Matsuno, pp. 104-123, Univ. of Tokyo, Tokyo.

- Neelin, J. D., and I. M. Held. 1987: Modeling Tropical Convergence Based on the Moist Static Energy Budget. *Monthly Weather Review*, 115, 3–12.
- Neelin J. D., I. M. Held, and K. H. Cook, 1987: Evaporation–wind feedback and low-frequency variability in the tropical atmosphere. *J. Atmos. Sci.*, **44**, 2341–2348.
- Numaguti, A., M. Takahashi, T. Nakajima, and A. Sumi, 1995: Development of an atmospheric general circulation model, in *Climate System Dynamics and Modelling*, vol. I-3, edited by T. Matsuno, pp. 1-27, Univ. of Tokyo, Tokyo.
- Oort, A. H., and J. J. Yienger, 1996: Observed long-term variability in the Hadley circulation and its connection to ENSO. *J. Climate*, **9**, 2751-2767.
- Qian T., 2003: Cloud vertical structure and radiative heating profiles during TOGA COARE. Ph.D. thesis, State University of New York at Stony Brook, 141 pp. [Available from State University of New York at Stony Brook, Stony Brook, NY 11794.].
- Raymond D. J., 2001: A new model of the Madden–Julian oscillation. *J. Atmos. Sci.*, **58**, 2807–2819.
- Roundy, P.E., and G. N. Kiladis, 2006: Observed relationships between intraseasonal oceanic Kelvin waves and atmospheric forcing. *J. Climate* 19, 5253-5272.
- Salby, M., and R. R. Garcia, 1987: Transient response to localized episodic heating in the tropics. Part I : Excitation and short-time near-field behavior. *J. Atmos. Sci.*, **44**, 458-498
- Schubert, S., R. Dole, H.v.d. Dool, M. Suarez, and D. Waliser, 2002: Proceedings from a workshop on "Prospects for improved forecasts of weather and short-term climate

- variability on subseasonal (2 week to 2 month) time scales”, 16-18 April 2002, Mitchellville, MD, NASA/TM 2002-104606, vol. 23, pp. 171.
- Slingo, J. M., and R. A. Madden, 1991: Characteristics of the tropical intraseasonal oscillation in the NCAR community climate model. *Q. J. R. Meteorol. Soc.*, **117**, 1129-1169.
- Slingo, J. M., and Coauthors, 1996: Intraseasonal oscillations in 15 atmospheric general circulation models: Results from an AMIP diagnostic subproject. *Climate Dyn.*, **12**, 325-357.
- Sobel A. H., and H. Gildor, 2003: A simple time-dependent model of SST hot spots. *J. Climate*, **16**, 3978–3992.
- Sobel, A. H., and C. S. Bretherton, 2000: Modeling tropical precipitation in a single column. *J. Climate.*, **13**, 4378–4392.
- Takayabu, Y. N., 1994: Large-scale cloud disturbances associated with equatorial waves. Part I: Spectral features of the cloud disturbances. *J. Meteor. Soc. Japan*, **72**, 433–448.
- Takayabu, Y. N., T. Iguchi, M. Kachi, A. Shibata, and H. Kanzawa, 1999: Abrupt termination of the 1997-98 El Nino in response to a Madden-Julian oscillation. *Nature*, **402**, 279-282.
- Tiedtke, M., 1983: The sensitivity of the time-mean large-scale flow to cumulus convection in the ECMWF model. *Workshop on Convection in Large-Scale Numerical Models*. ECMWF, 28 Nov-1 Dec 1983, pp297-316.
- Tiedke, M., 1989: A comprehensive mass flux scheme for cumulus parameterization in large-scale models. *Mon. Wea. Rev.*, **117**, 1779-1800.

- Tokioka, T., K. Yamazaki, A. Kitoh, and T. Ose, 1988: The equatorial 30-60-day oscillation and the Arakawa-Schubert penetrative cumulus parameterization. *J. Meteor. Soc. Japan*, **66**, 883-901.
- Waliser, D., S. Schubert, A. Kumar, K. Weickmann, and R. Dole, 2003: Proceedings from a workshop on "Modeling, Simulation and Forecasting of Subseasonal Variability", NASA/CP 2003-104606, vol. 25, pp. 62.
- Wang B., and H. Rui, 1990: Dynamics of the coupled moist Kelvin–Rossby wave on an equatorial β -plane. *J. Atmos. Sci.*, **47**, 398–413.
- Wang, W., and M.E. Schlesinger, 1999: The dependence on convective parameterization of the tropical intraseasonal oscillation simulated by the UIUC 11-layer atmospheric GCM. *J. Climate*, **12**, 1423-1457.
- Weickmann, K. M., G. R. Lussky, and J. E. Kutzbach, 1985: Intraseasonal (30-60 day) fluctuations of outgoing longwave radiation and 250 mb streamfunction during northern winter. *Mon. Wea. Rev.*, **113**, 941-961.
- Weickmann, K., G. Kiladis and P. Sardeshmukh, 1997: The dynamics of intraseasonal atmospheric angular momentum oscillations. *J. Atmos. Sci.*, **54**, 1445-1461.
- Wheeler, M., and G.N. Kiladis, 1999: Convectively Coupled Equatorial Waves: Analysis of Clouds and Temperature in the Wavenumber-Frequency Domain. *J. Atmos. Sci.*, **56**, 374-399.
- Wheeler, M., G.N. Kiladis, and P.J. Webster, 2000: Large-scale dynamical fields associated with convectively coupled equatorial waves. *J. Atmos. Sci.*, **57**, 613-640.

- Wheeler, M.C., and J.L. McBride, 2005: Australian-Indonesian monsoon. *Intraseasonal Variability in the Atmosphere-Ocean Climate System*. W.K.M. Lau and D.E. Waliser (Eds.), Praxis Publishing, pp 125-173.
- Yasunari, T., 1979: Cloudiness fluctuations associated with the northern hemisphere summer monsoon. *J. Meteor. Soc. Japan*, **57**, 227-242.
- Yuter, S. E., and R. A. Houze Jr., 2000: The 1997 Pan American Climate Studies Tropical Eastern Pacific Process Study. Part I: ITCZ Region. *Bulletin of the American Meteorological Society*, 81, 451–481.

FIGURE CAPTIONS

Figure 1. Annual mean precipitation along the equatorial belt averaged between (a) 15N and 15S, and (b) 5N and 5S for two observational datasets and each model experiment. The data are smoothed zonally to keep only wavenumber 0-6. The locations of continents within the equatorial belt are indicated by black bars under the abscissa.

Figure 2. Height-longitude cross section of EXP2-EXP7 difference in annual mean (a) cloud fraction, (b) longwave heating, (c) shortwave heating, and (d) total radiative heating averaged between 20N-20S.

Figure 3. Same as Figure 2 but for (a) convective heating, (b) large-scale condensational heating, (c) total heating due to moist processes, and (d) total diabatic heating.

Figure 4. Same as Figure 2 but for (a) temperature, and (b) specific humidity.

Figure 5. Variance of the 2-128 day precipitation anomaly along the equator averaged between 15N-15S.

Figure 6. Space-time spectrum of 15N-15S symmetric component of precipitation divided by the background spectrum. Superimposed are the dispersion curves of the odd meridional mode-numbered equatorial waves for the five equivalent depths of 12, 25, and 50m. Frequency spectral width is 1/128 cpd.

Figure 7. As in Figure 6 except for 15N-15S antisymmetric component of precipitation.

Figure 8. Variances of (a) MJO, (b) Kelvin, (c) $n=1$ ER, (d) MRG, (e) $n=0$ EIG, and (f) $n=1$ WIG modes along the equator averaged between 15N and 15S.

Figure 9. Linear regression against surface total precipitation for (a) cloud fraction, (b) shortwave heating, (c) longwave heating, and (d) total radiative heating.

Figure 10. Same as Figure 9 but for (a) convective heating, (b) large-scale condensational heating, (c) total heating due to moist processes, and (d) total diabatic heating (moist processes plus radiation).

Figure 11. (a) Effective static stability, (b) dry static stability, and (c) reduction term due to diabatic heating.

Figure 12. Lag-regression against the Kelvin wave precipitation anomaly in EXP7 for (a) cloud amount $[\%/(mm/day)]$, (c) longwave heating rate $[(W/m^2)/(mm/day)]$, (e) shortwave heating rate $[(W/m^2)/(mm/day)]$, (g) total radiative heating rate $[(W/m^2)/(mm/day)]$, (i) heating due to moist processes $[(W/m^2)/(mm/day)]$, (k) total diabatic heating $[(W/m^2)/(mm/day)]$, and (m) omega $[(mb/day)/(mm/day)]$. All data are area-averaged between 5N-5S, 150-160E. The corresponding structures for EXP2 are shown in (b), (d), (f), (h), (j), (l) and (n), respectively. The first contour is 5×10^{-3} , 2×10^{-2} , 2×10^{-2} , 2×10^{-2} , 1×10^{-1} , 1×10^{-1} and 2×10^{-5} , while contour interval is 1×10^{-2} , 2×10^{-2} , 2×10^{-2} , 2×10^{-2} , 2×10^{-1} , 2×10^{-1} and 4×10^{-5} , respectively. Shading denotes the regions where the corresponding lag-correlation is above the 95% confidence level, with dark (light) shading for positive (negative) lag-correlation.

Figure 13. Same as Figure 12 but for the MJO.

Figure 14. (a) Annual mean OLR, and (b) Linear regression of daily -OLR vs precipitation along the equator averaged between 5N-5S for observation and model experiments. In (b) same unit is used for both variables so that the regression coefficient is unitless.

Table 1. Description of sensitivity experiments

Experiment	Autoconversion timescale (seconds)
EXP8	19200
EXP7 (CNTL)	9600
EXP6	6400
EXP5	3200
EXP4	1600
EXP3	800
EXP2	400
EXP1	200
EXP0 (NO CLOUD)	0

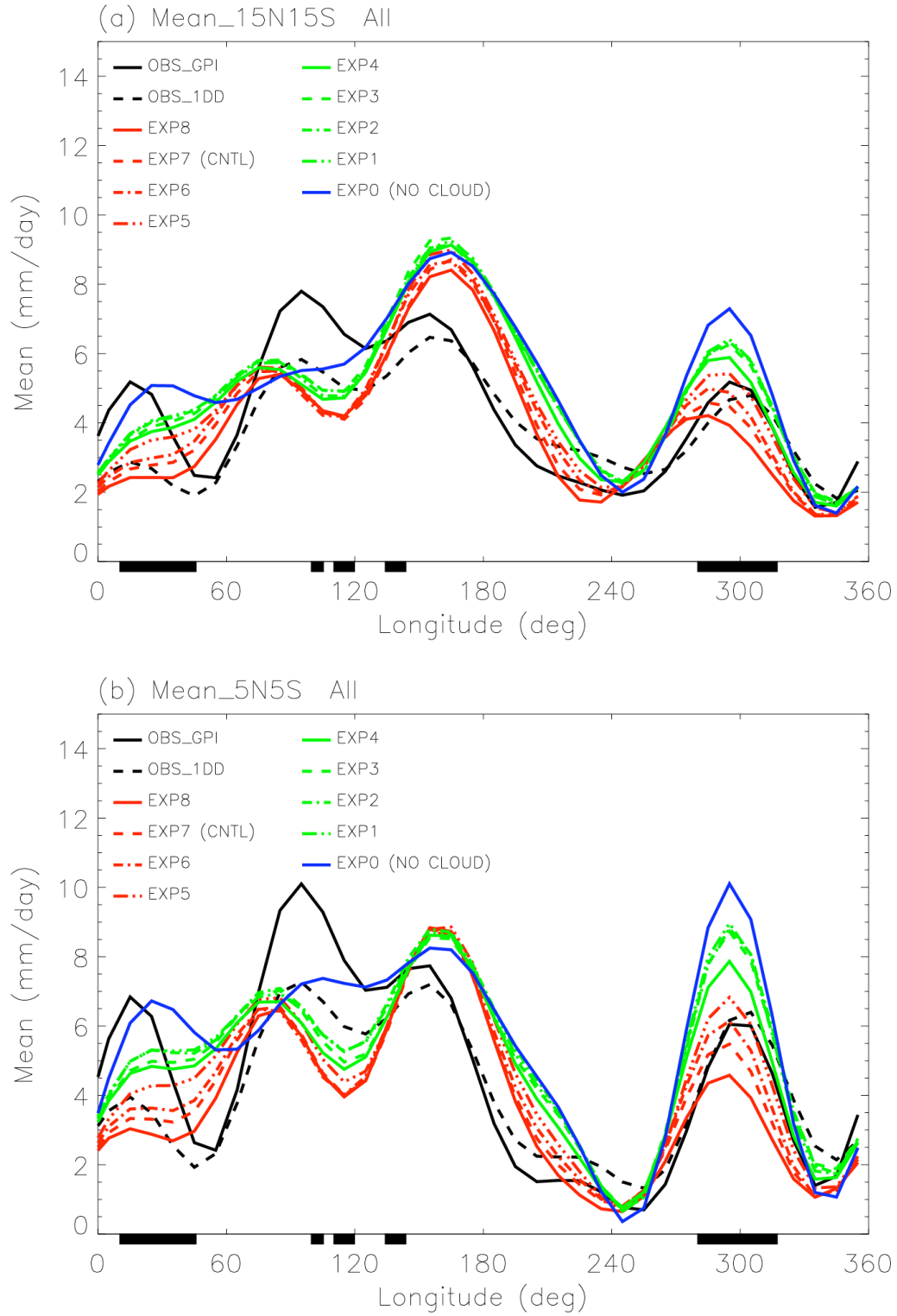


Figure 1. Annual mean precipitation along the equatorial belt averaged between (a) 15N and 15S, and (b) 5N and 5S for two observational datasets and each model experiment. The data are smoothed zonally to keep only wavenumber 0-6. The locations of continents within the equatorial belt are indicated by black bars under the abscissa.

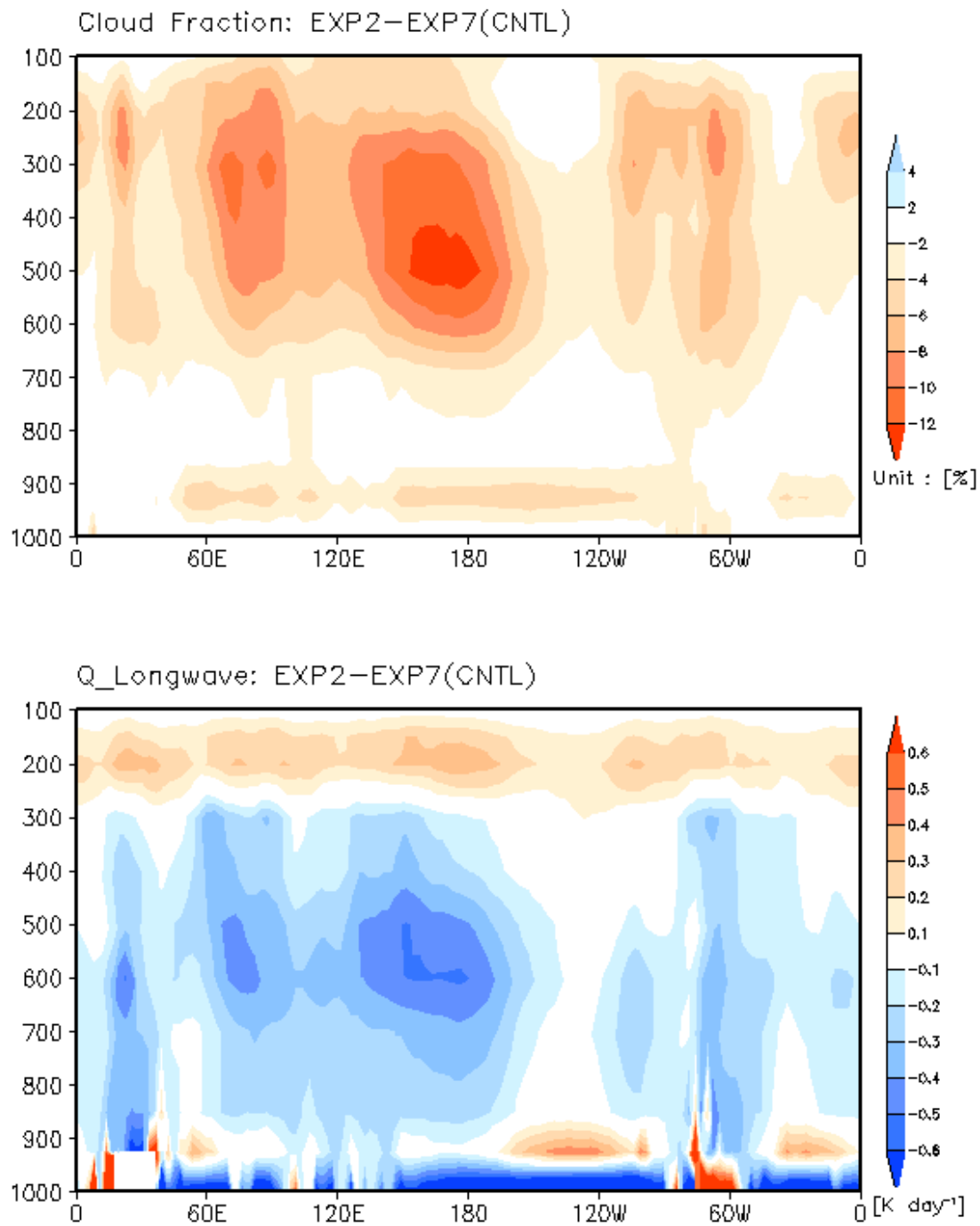
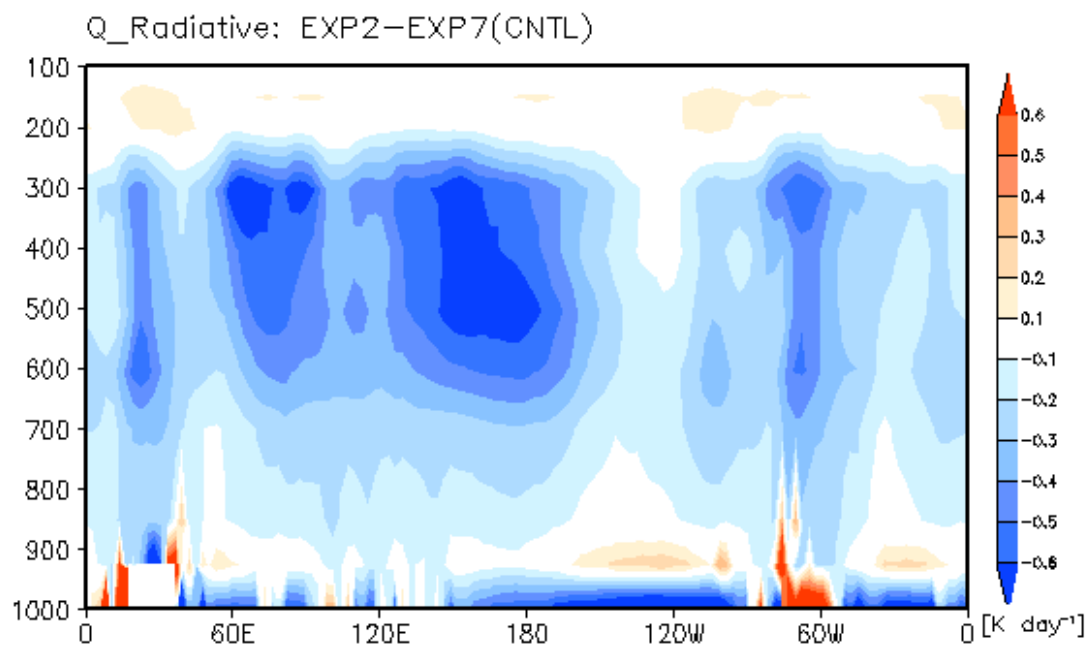
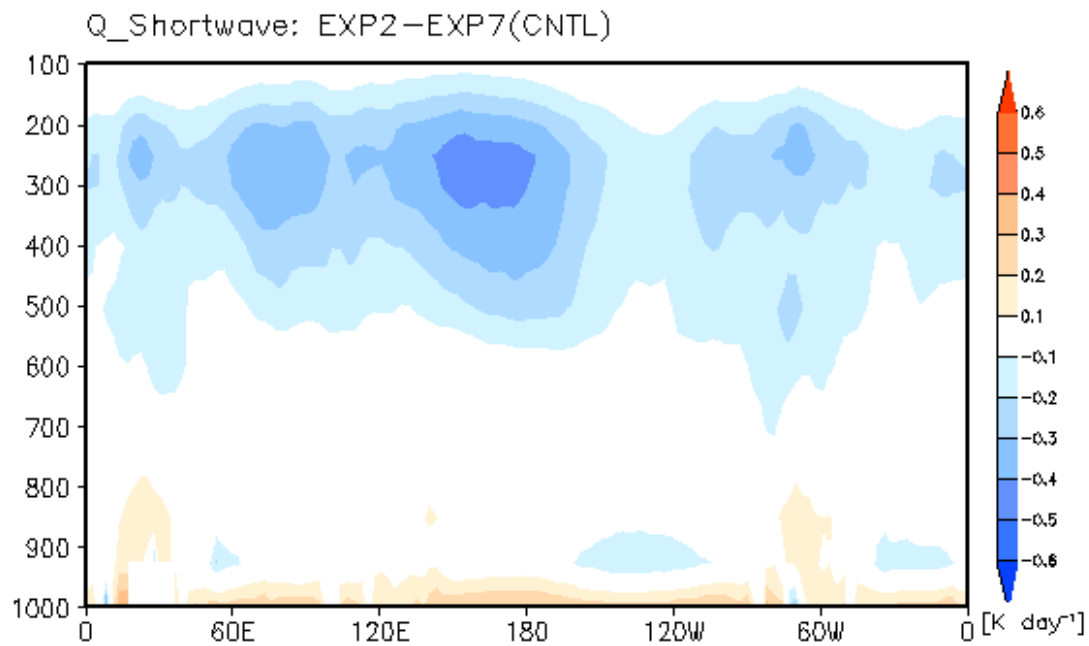


Figure 2. Height-longitude cross section of EXP2-EXP7 difference in annual mean (a) cloud fraction, (b) longwave heating, (c) shortwave heating, and (d) total radiative heating averaged between 20N-20S.



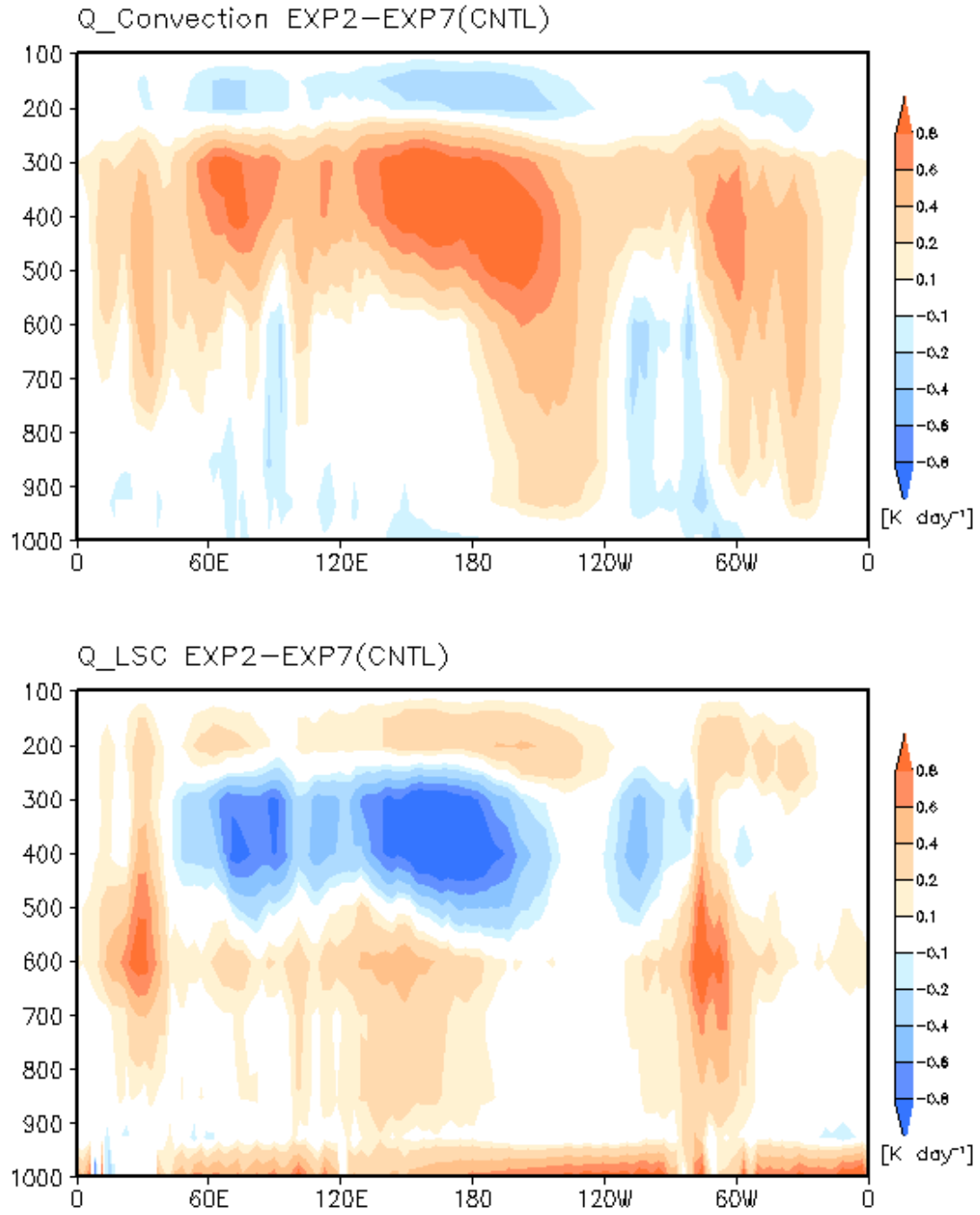
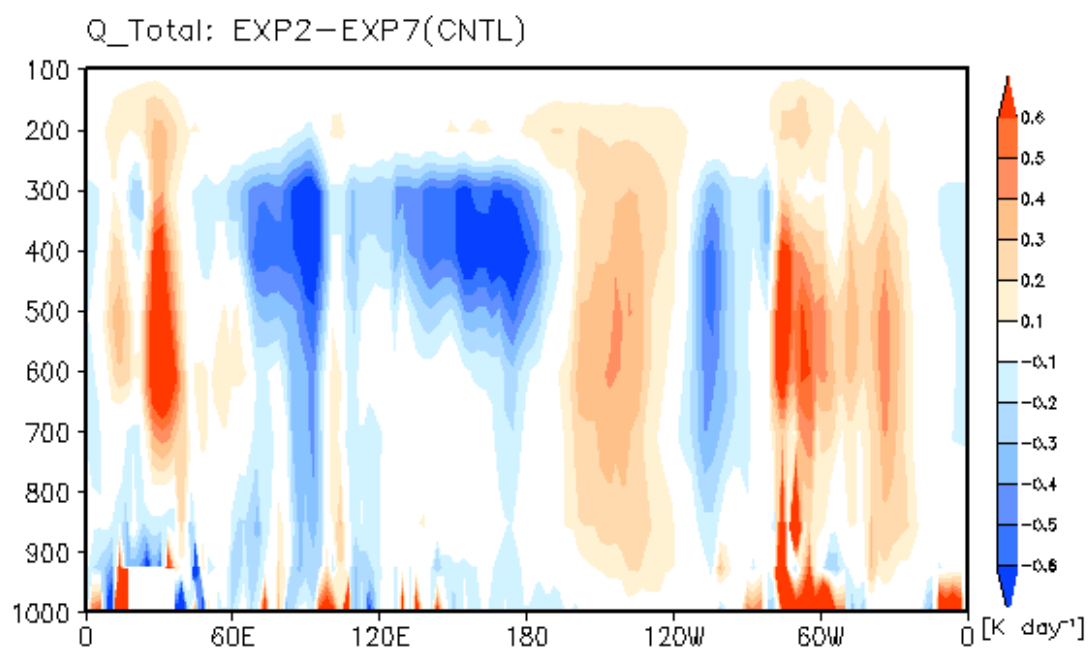
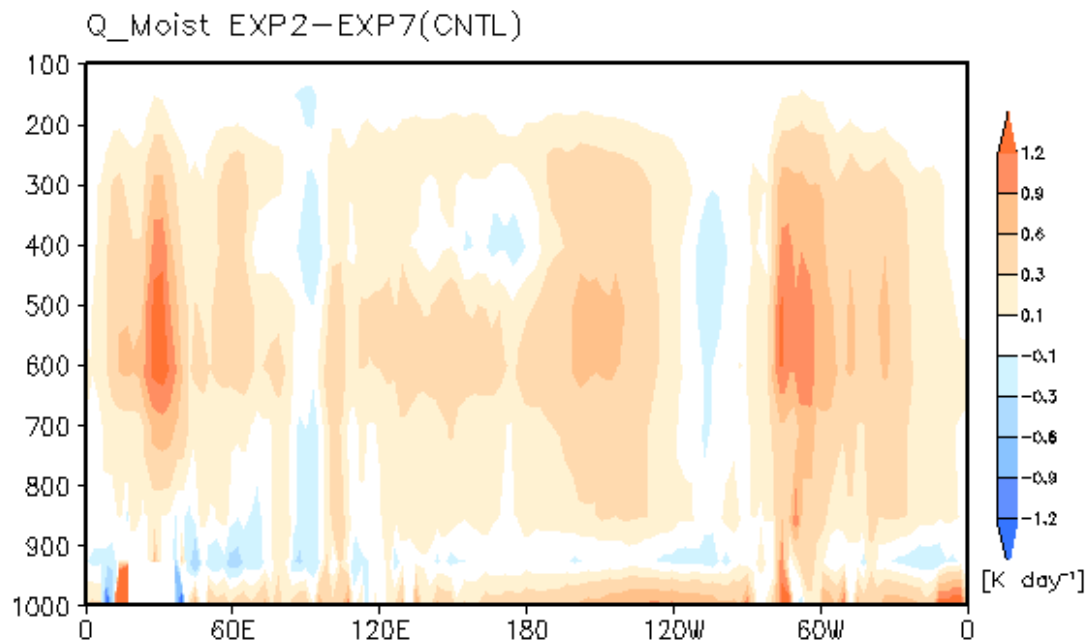


Figure 3. Same as Figure 2 but for (a) convective heating, (b) large-scale condensational heating, (c) total heating due to moist processes, and (d) total diabatic heating.



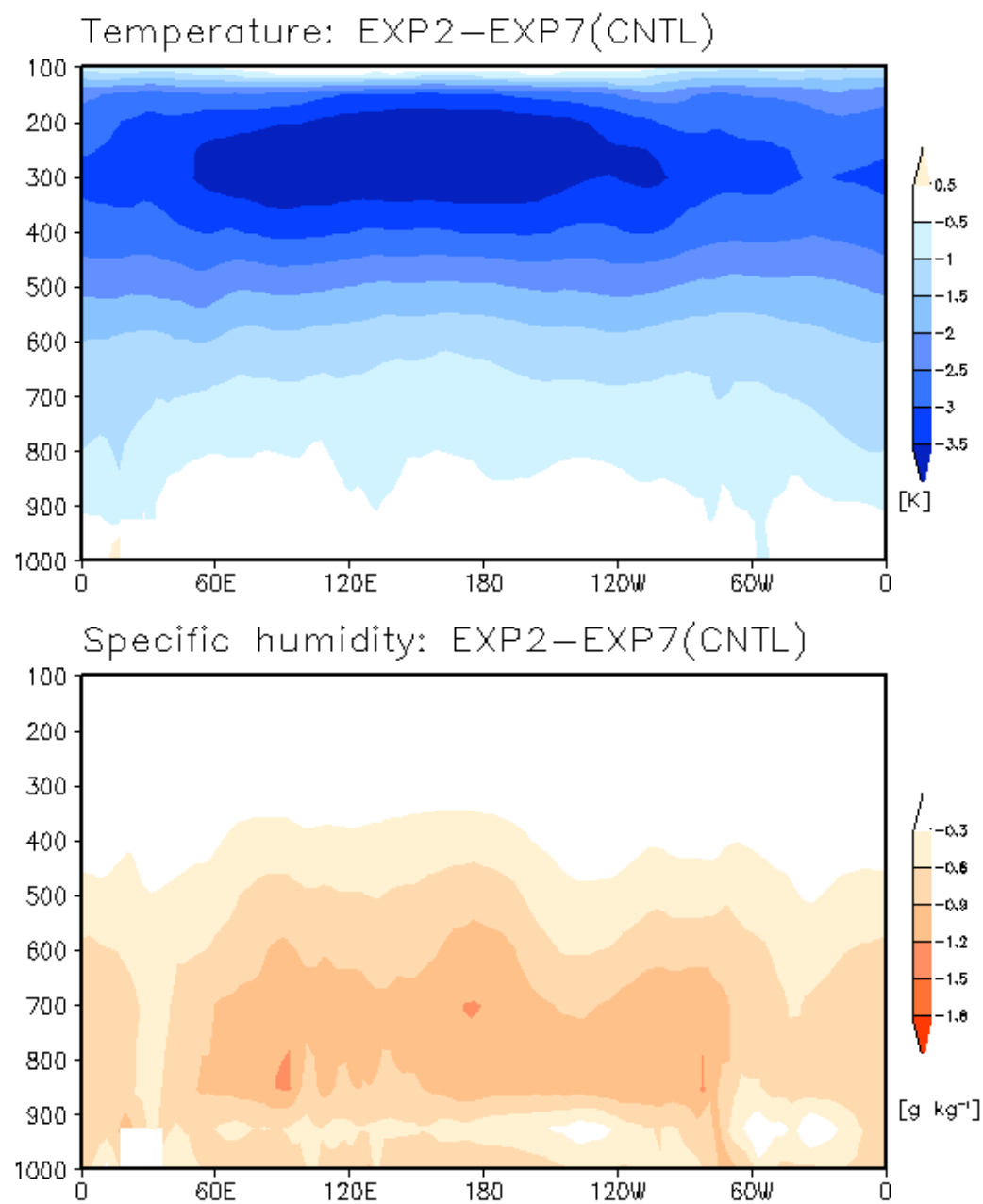


Figure 4. Same as Figure 2 but for (a) temperature, and (b) specific humidity.

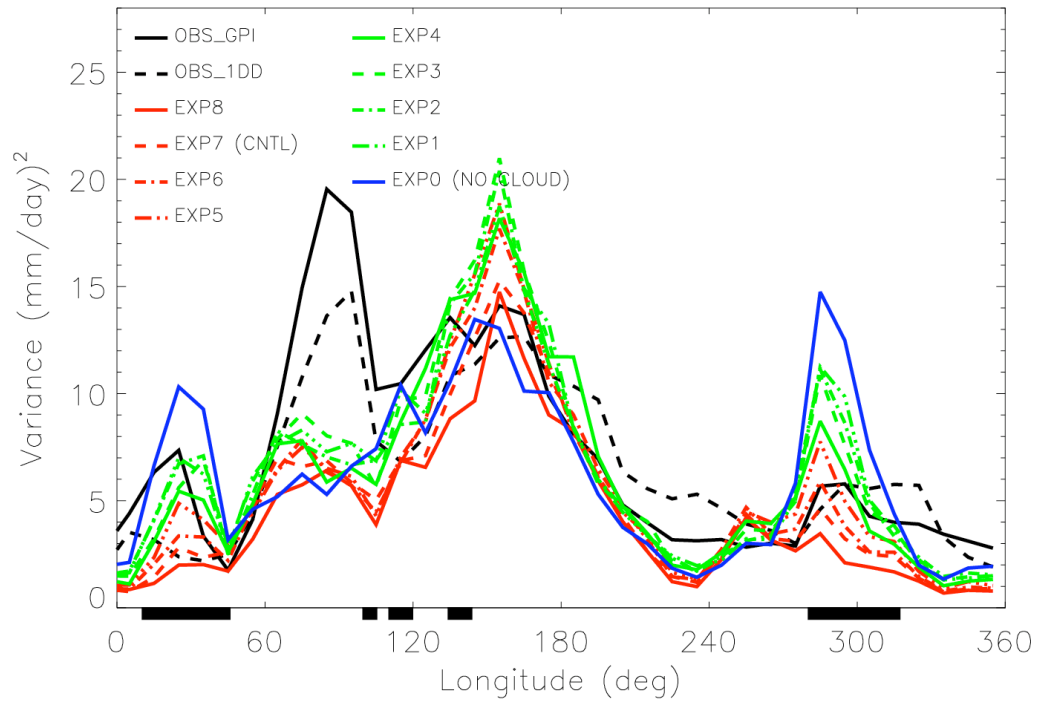


Figure 5. Variance of the 2-128 day precipitation anomaly along the equator averaged between 15N-15S.

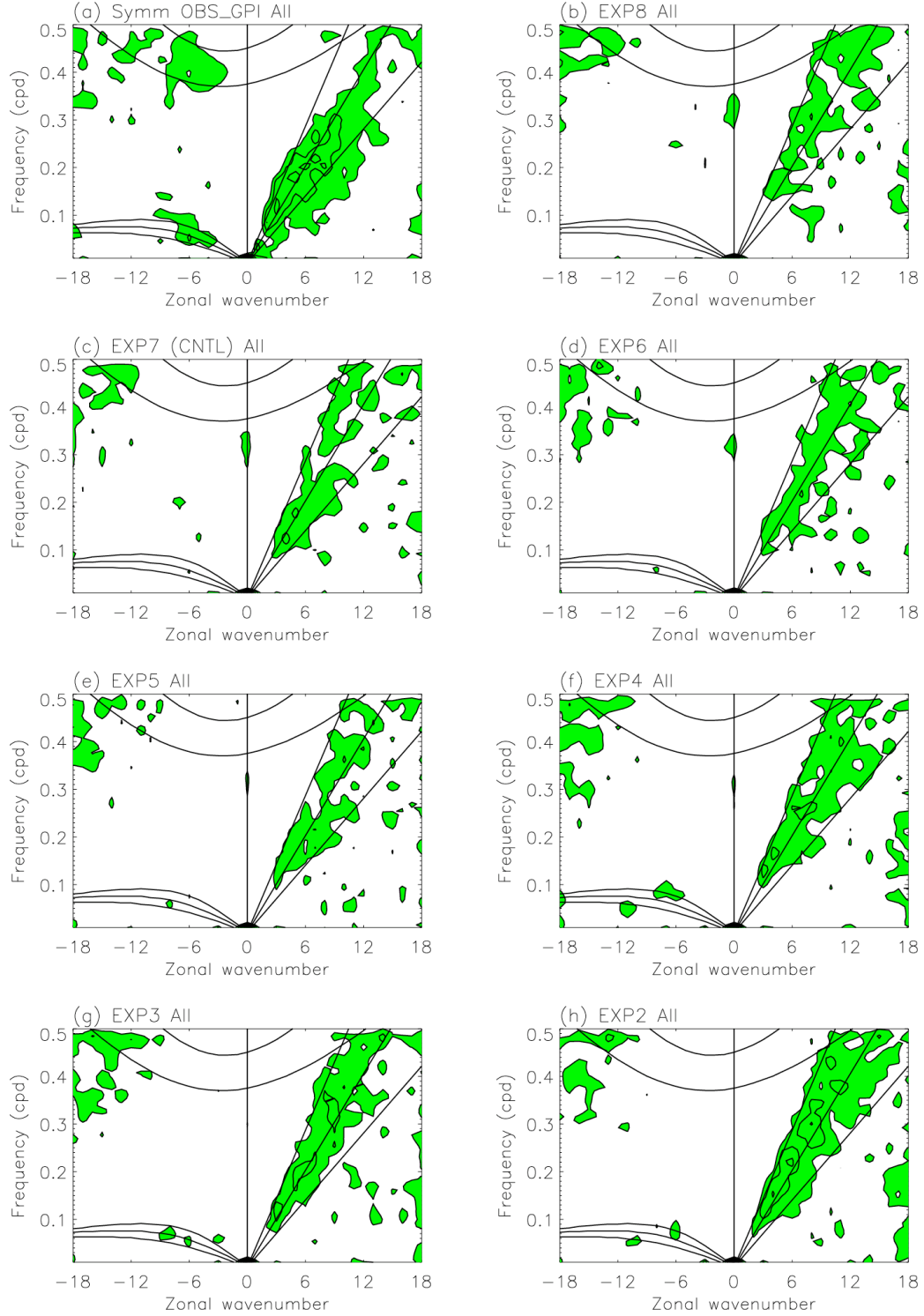


Figure 6. Space-time spectrum of 15N-15S symmetric component of precipitation divided by the background spectrum. Superimposed are the dispersion curves of the odd meridional mode-numbered equatorial waves for the five equivalent depths of 12, 25, and 50m. Frequency spectral width is 1/128 cpd.

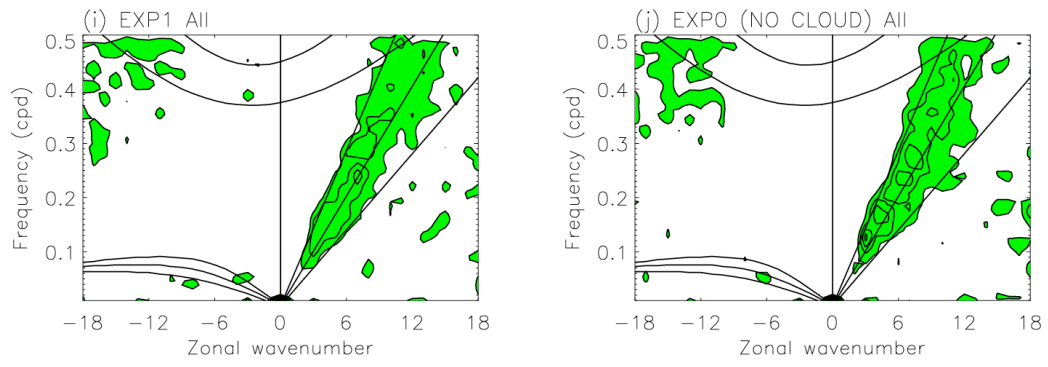


Figure 6. Continued.

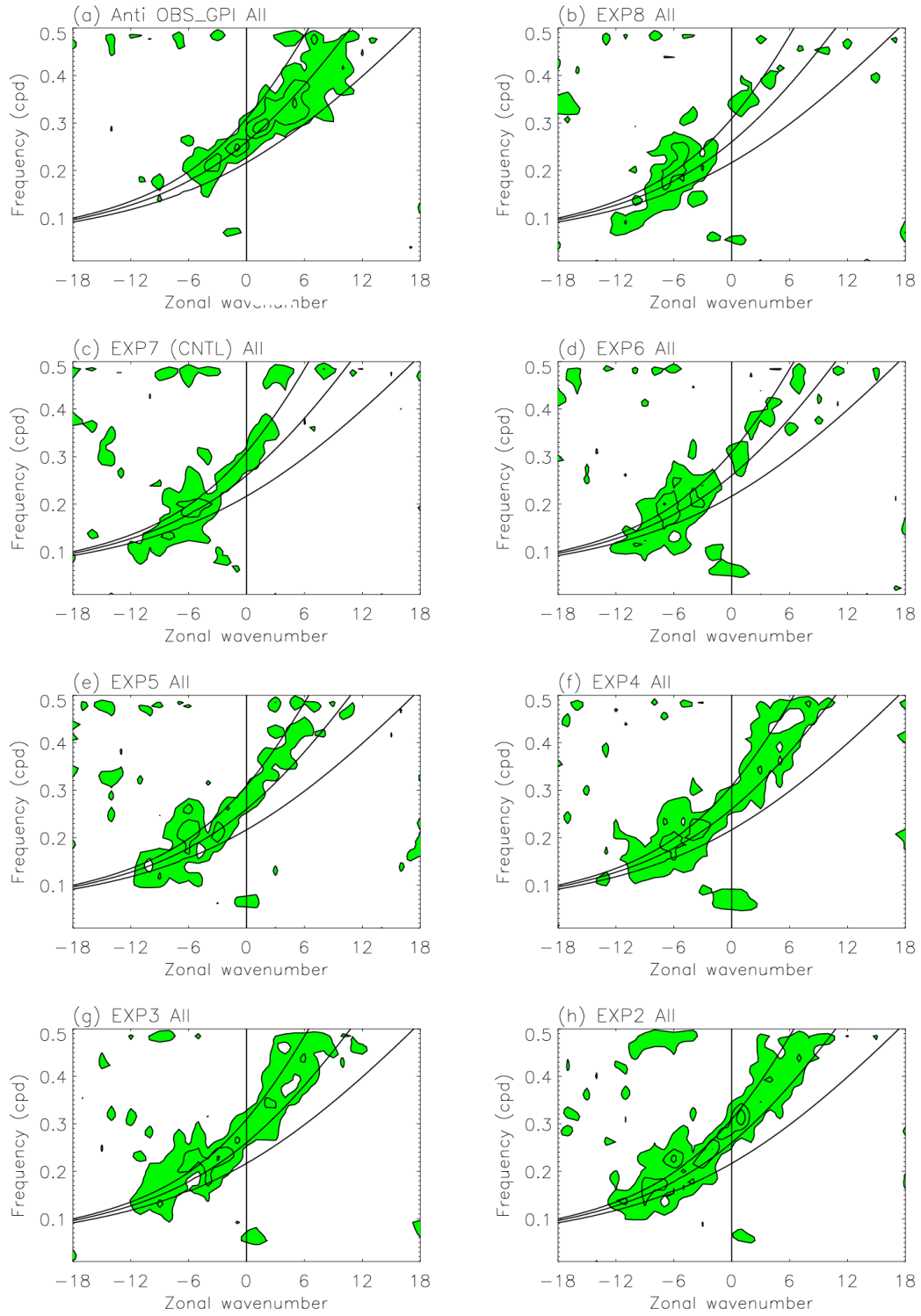


Figure 7. As in Figure 6 except for 15N-15S antisymmetric component of precipitation.

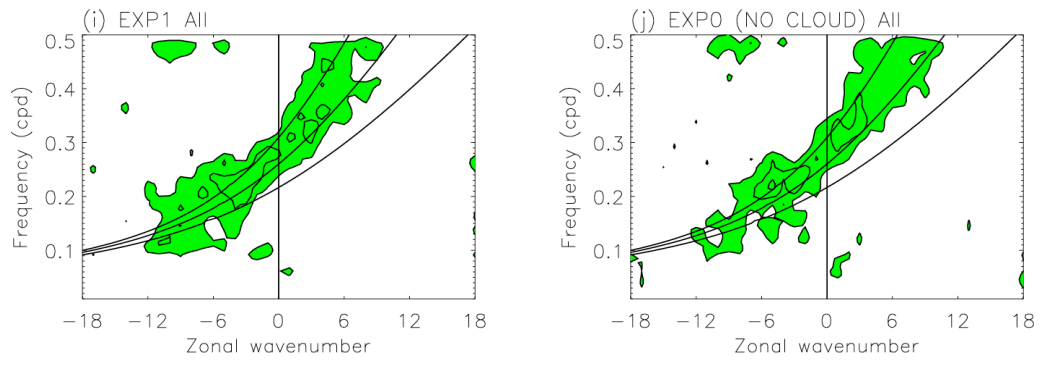


Figure 7. Continued.

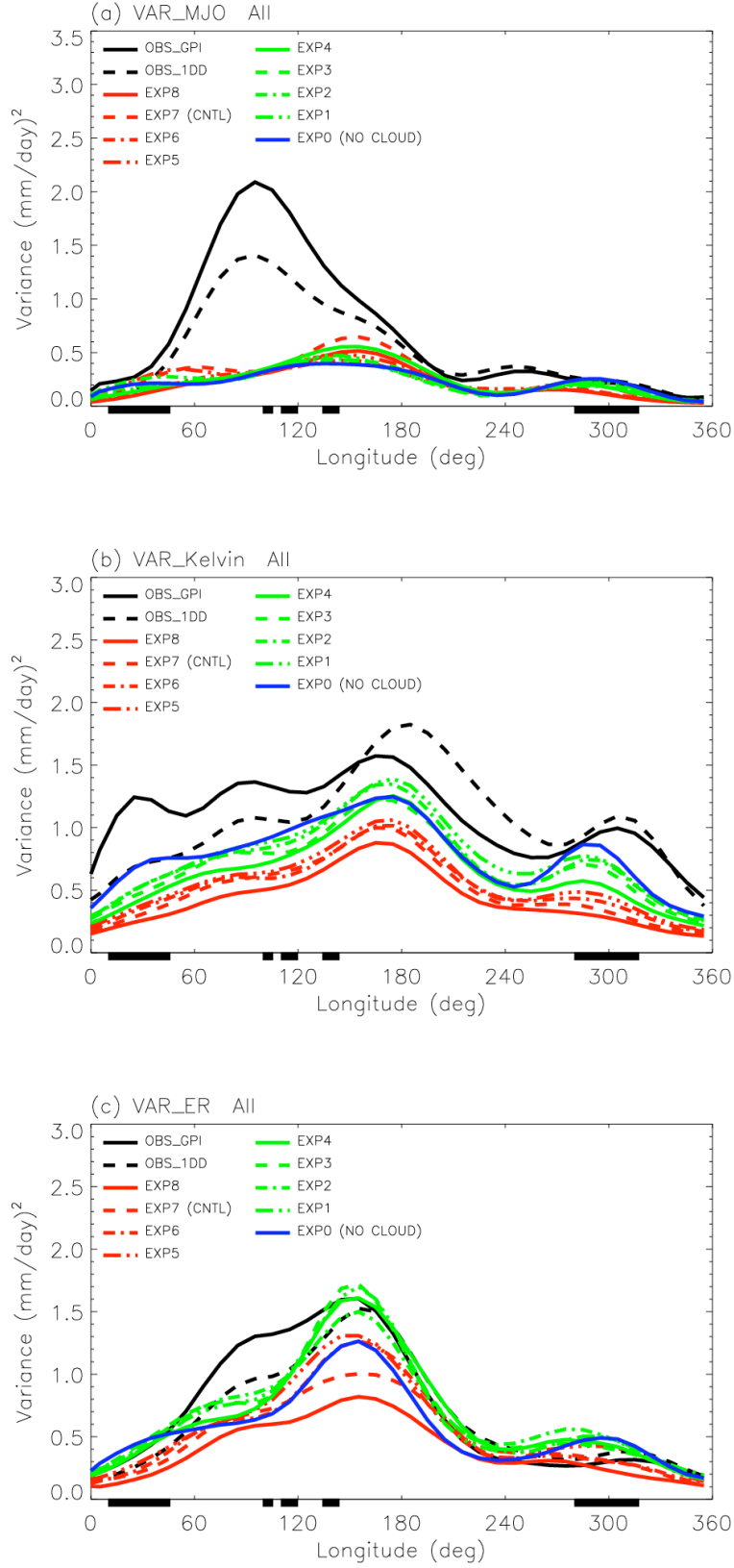
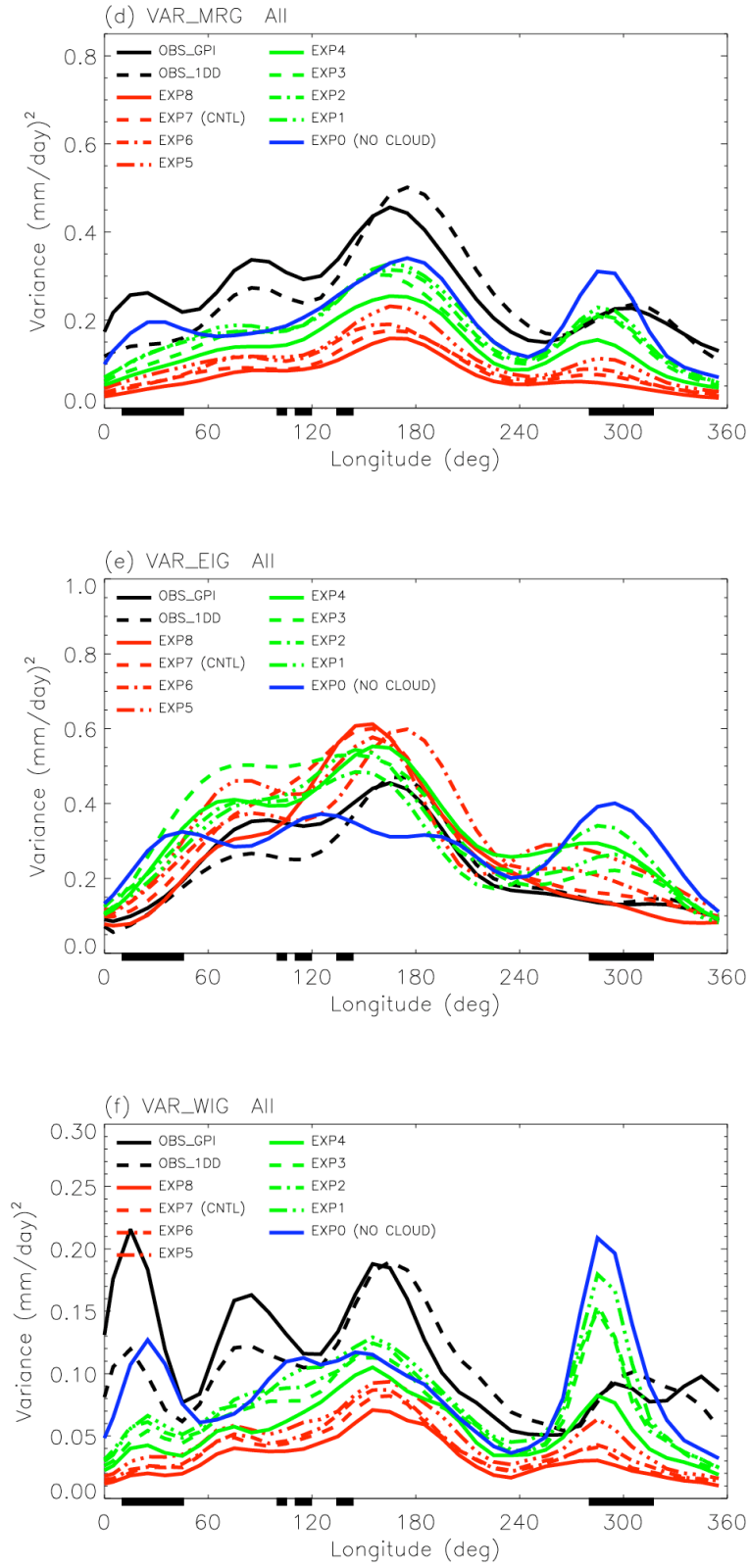


Figure 8. Variances of (a) MJO, (b) Kelvin, (c) $n=1$ ER, (d) MRG, (e) $n=0$ EIG, and (f) $n=1$ WIG modes along the equator averaged between 15N and 15S.



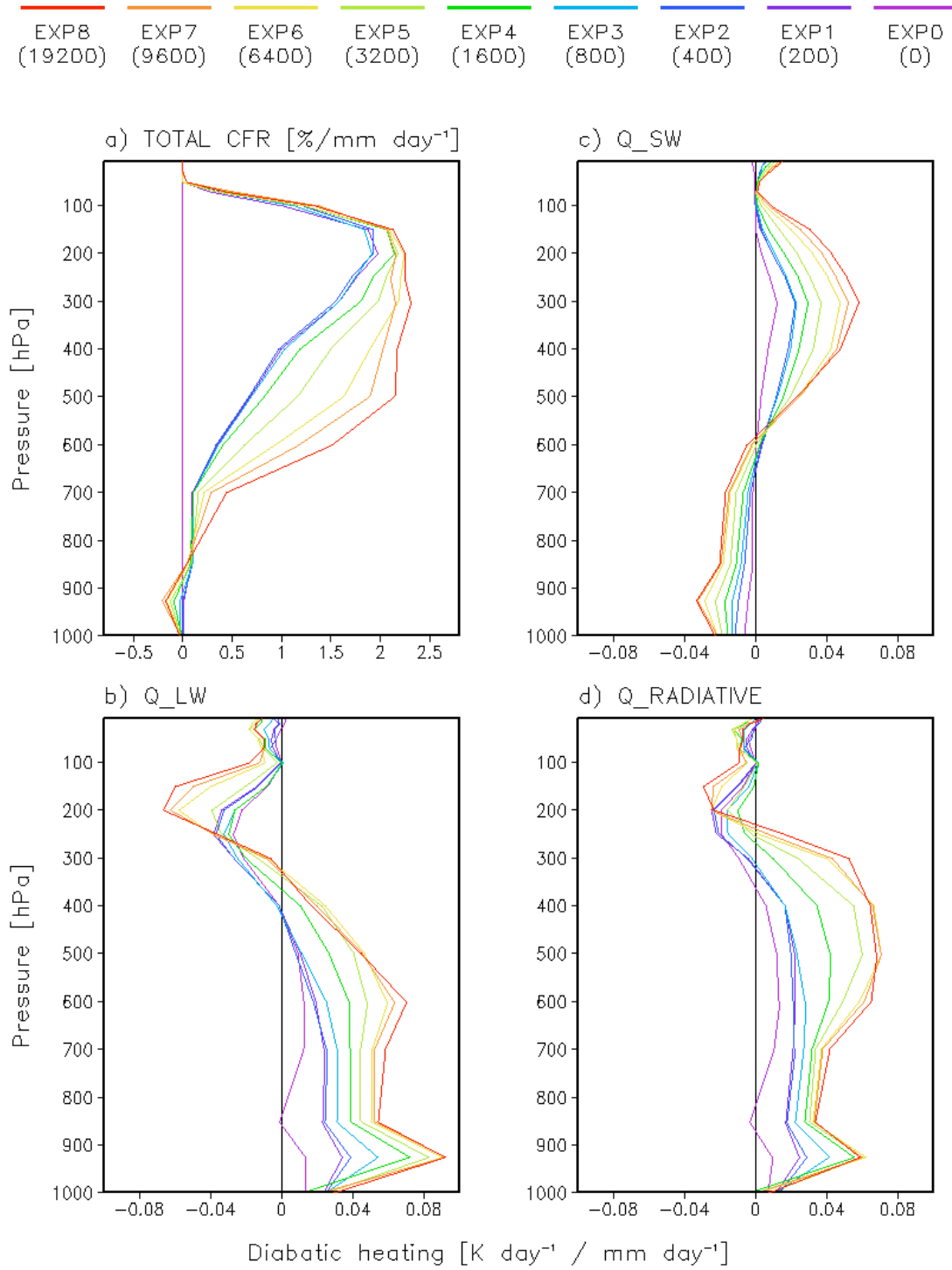


Figure 9. Linear regression against surface total precipitation for (a) cloud fraction, (b) shortwave heating, (c) longwave heating, and (d) total radiative heating.

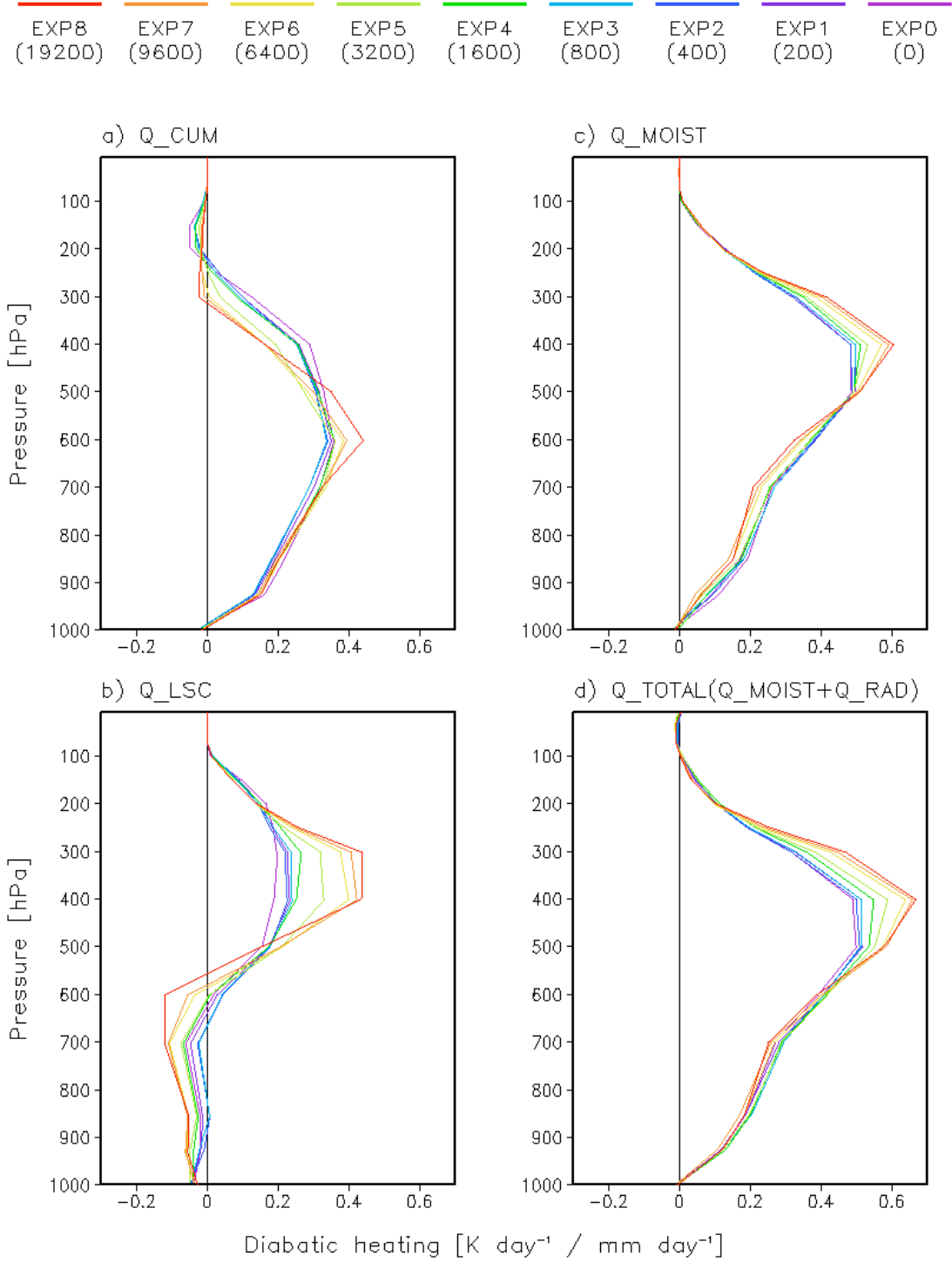


Figure 10. Same as Figure 9 but for (a) convective heating, (b) large-scale condensational heating, (c) total heating due to moist processes, and (d) total diabatic heating (moist processes plus radiation).

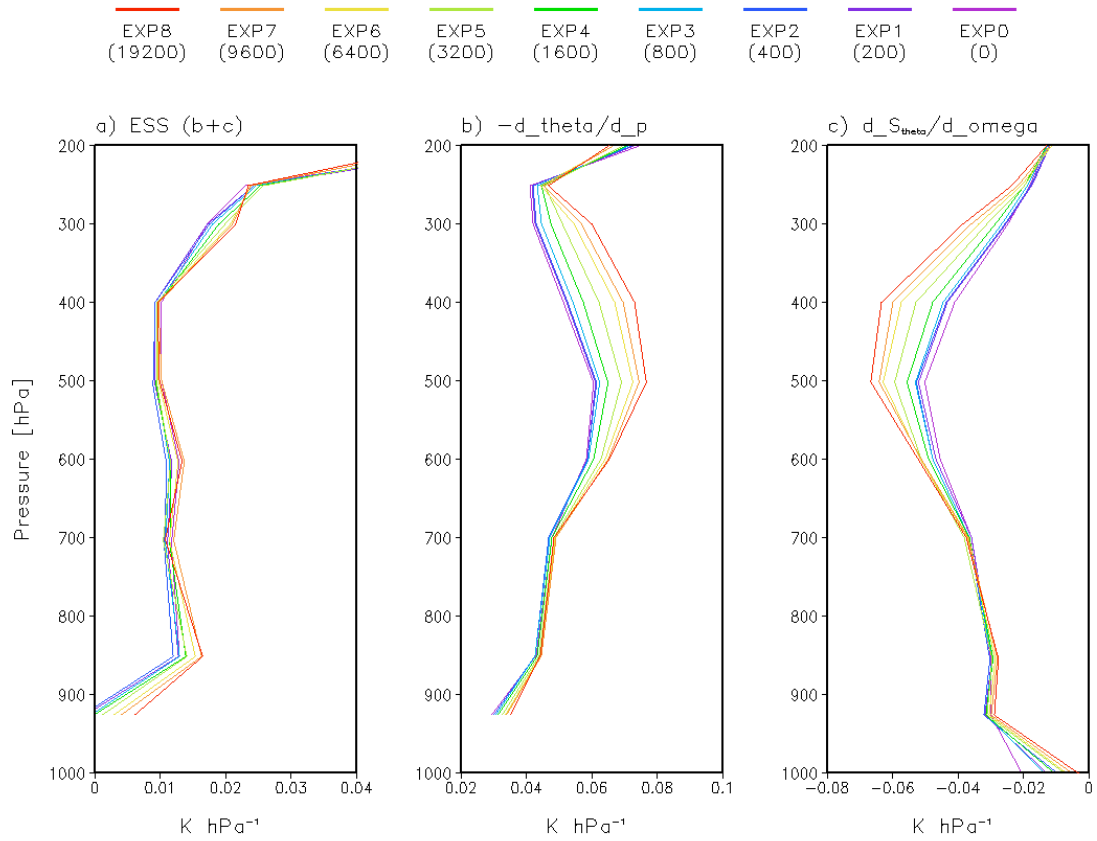


Figure 11. (a) Effective static stability, (b) dry static stability, and (c) reduction term due to diabatic heating.

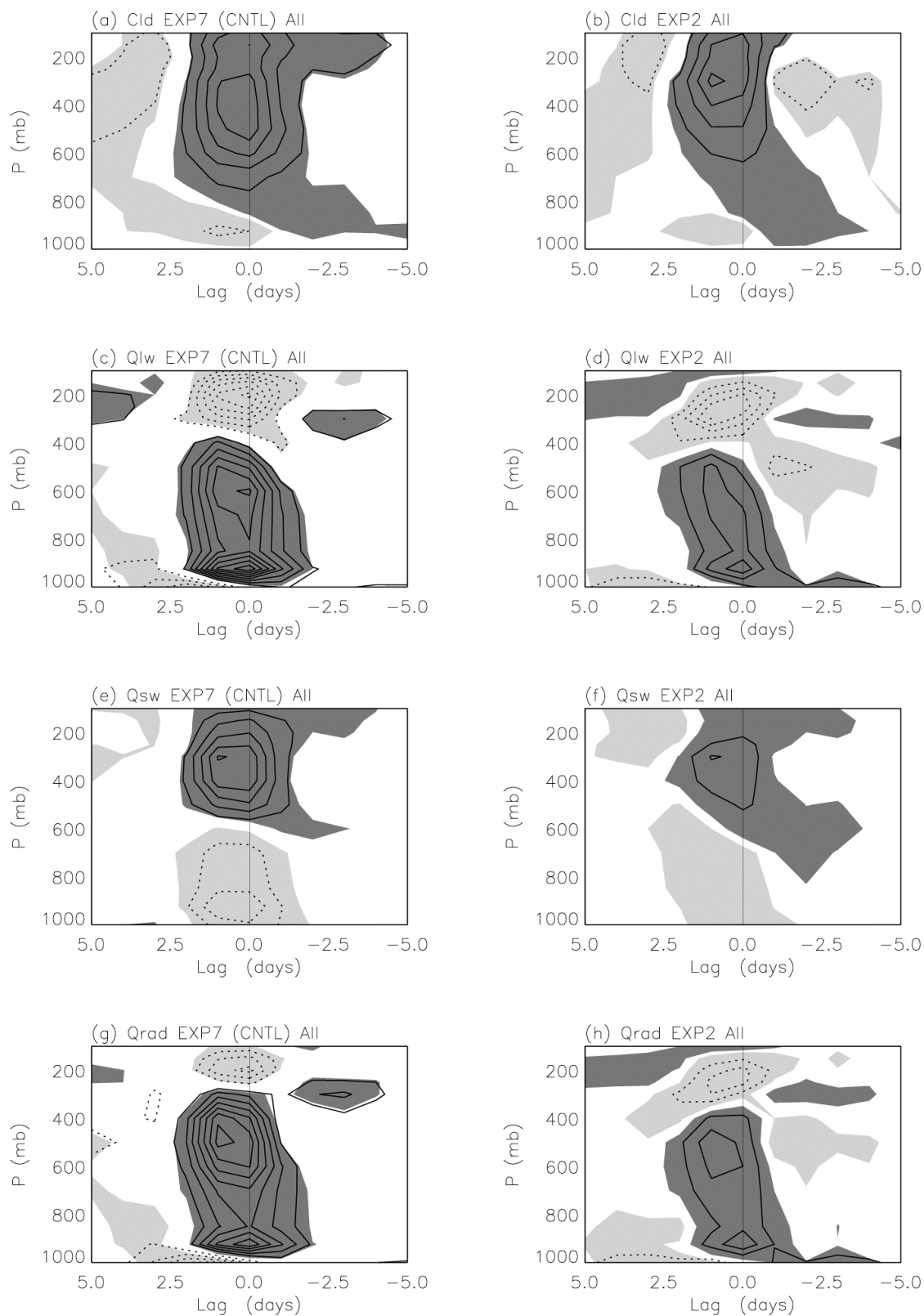


Figure 12. (see caption on the next page)

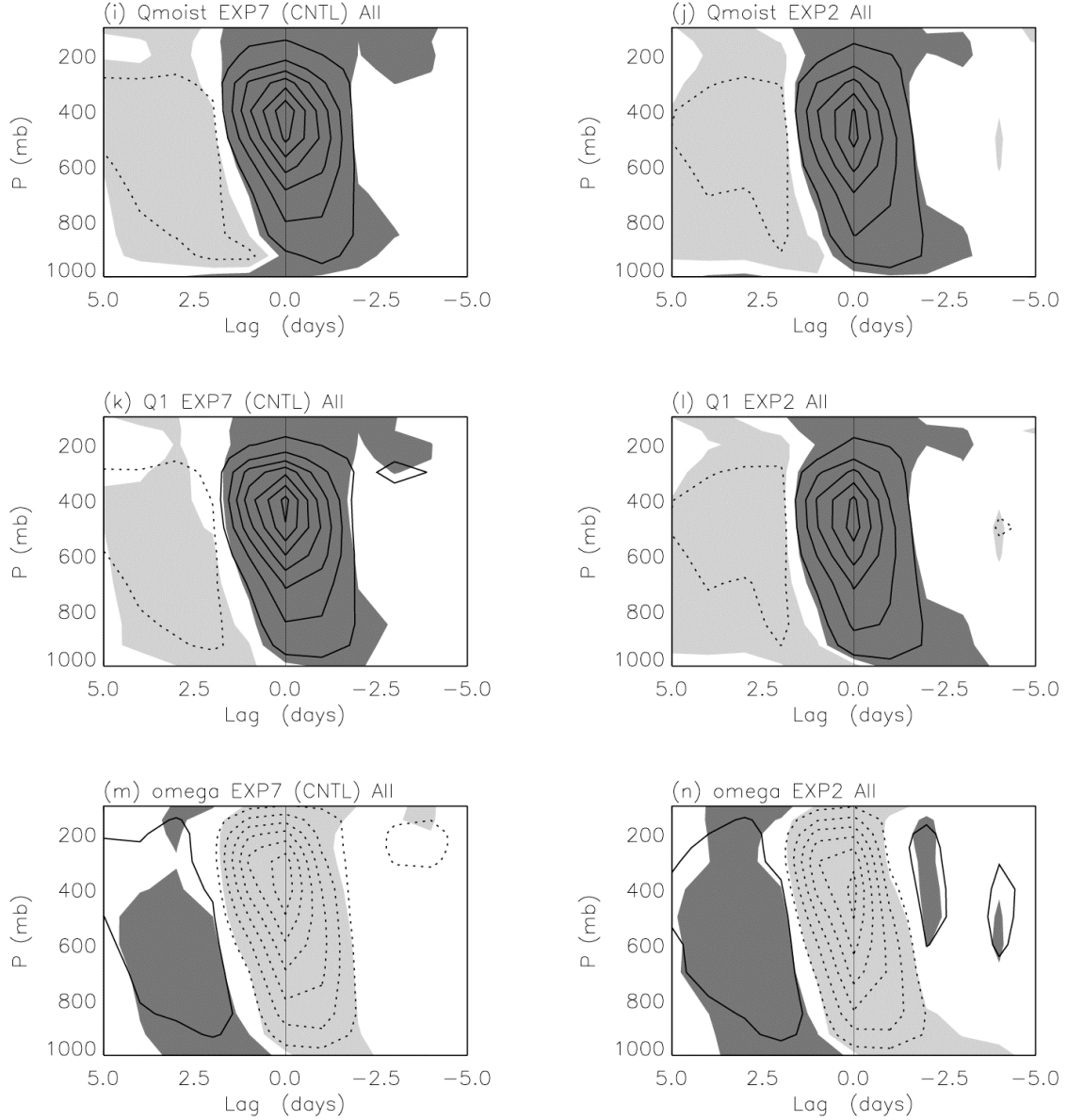


Figure 12. Lag-regression against the Kelvin wave precipitation anomaly in EXP7 for (a) cloud amount [$\% / (\text{mm/day})$], (c) longwave heating rate [$(\text{W/m}^2) / (\text{mm/day})$], (e) shortwave heating rate [$(\text{W/m}^2) / (\text{mm/day})$], (g) total radiative heating rate [$(\text{W/m}^2) / (\text{mm/day})$], (i) heating due to moist processes [$(\text{W/m}^2) / (\text{mm/day})$], (k) total diabatic heating [$(\text{W/m}^2) / (\text{mm/day})$], and (m) omega [$(\text{mb/day}) / (\text{mm/day})$]. All data are area-averaged between 5N-5S, 150-160E. The corresponding structures for EXP2 are shown in (b), (d), (f), (h), (j), (l) and (n), respectively. The first contour is 5×10^{-3} , 2×10^{-2} , 2×10^{-2} , 2×10^{-2} , 1×10^{-1} , 1×10^{-1} and 2×10^{-5} , while contour interval is 1×10^{-2} , 2×10^{-2} , 2×10^{-2} , 2×10^{-2} , 2×10^{-1} , 2×10^{-1} and 4×10^{-5} , respectively. Shading denotes the regions where the corresponding lag-correlation is above the 95% confidence level, with dark (light) shading for positive (negative) lag-correlation.

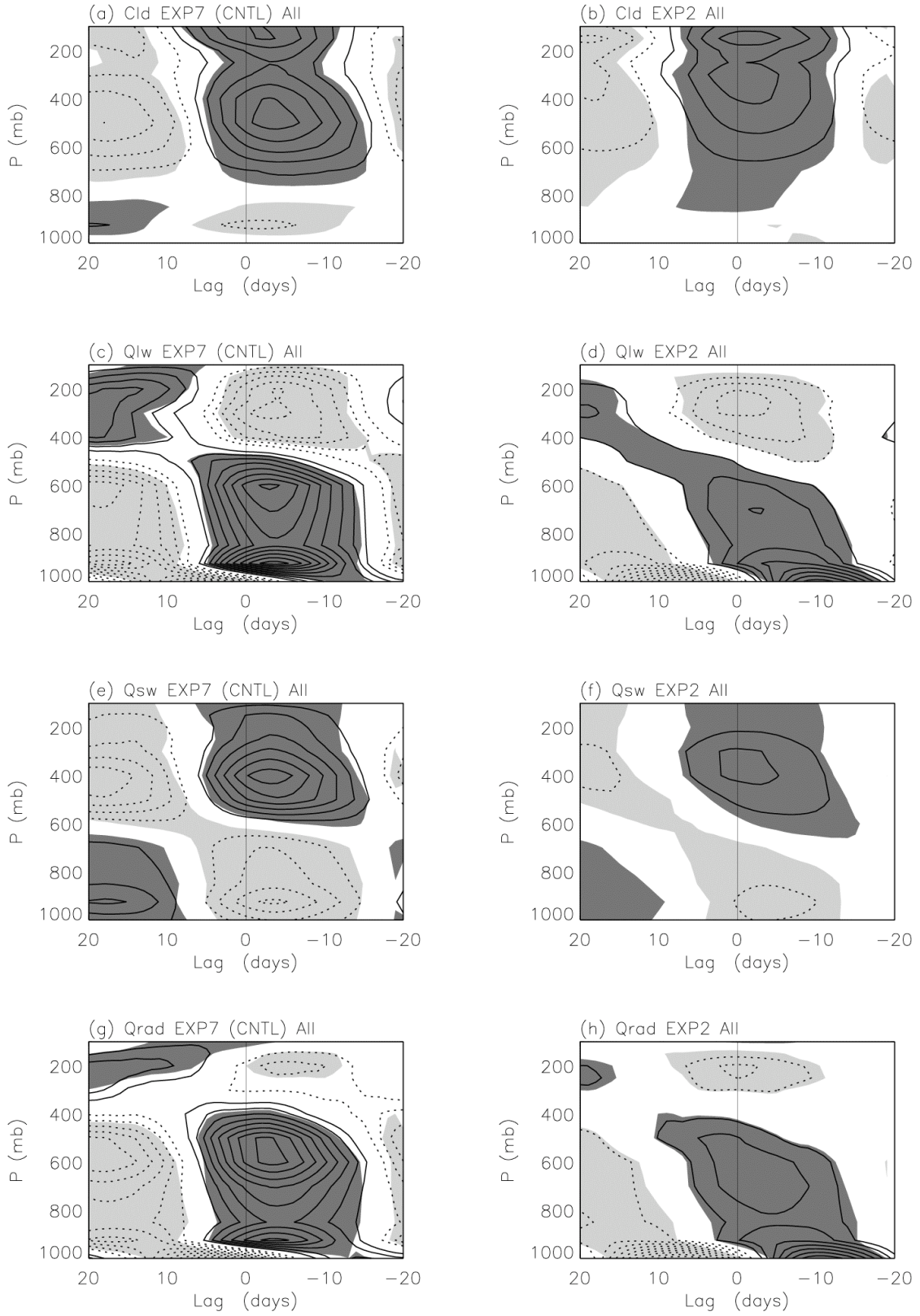


Figure 13. Same as Figure 12 but for the MJO.

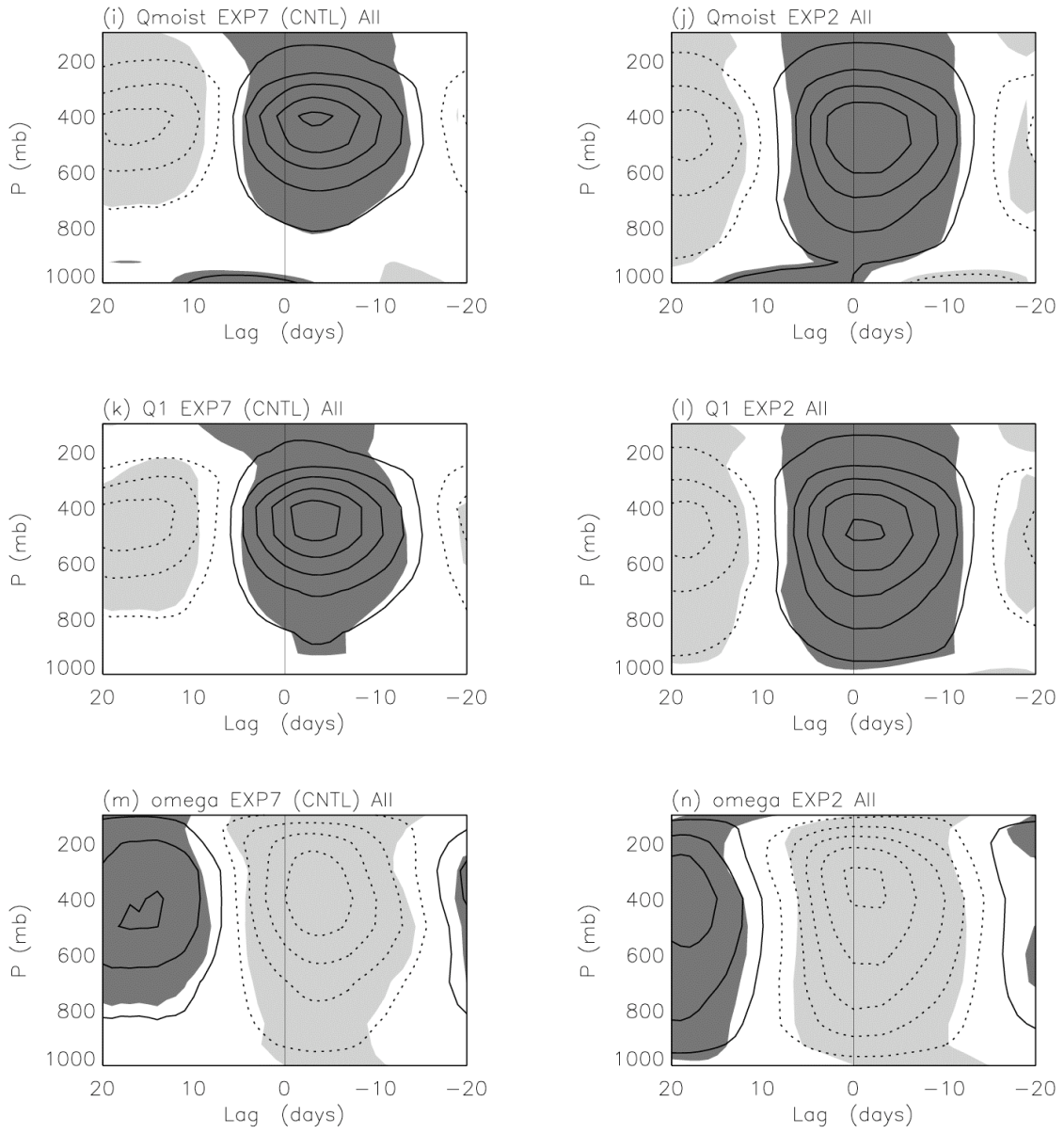


Figure 13. Continued.

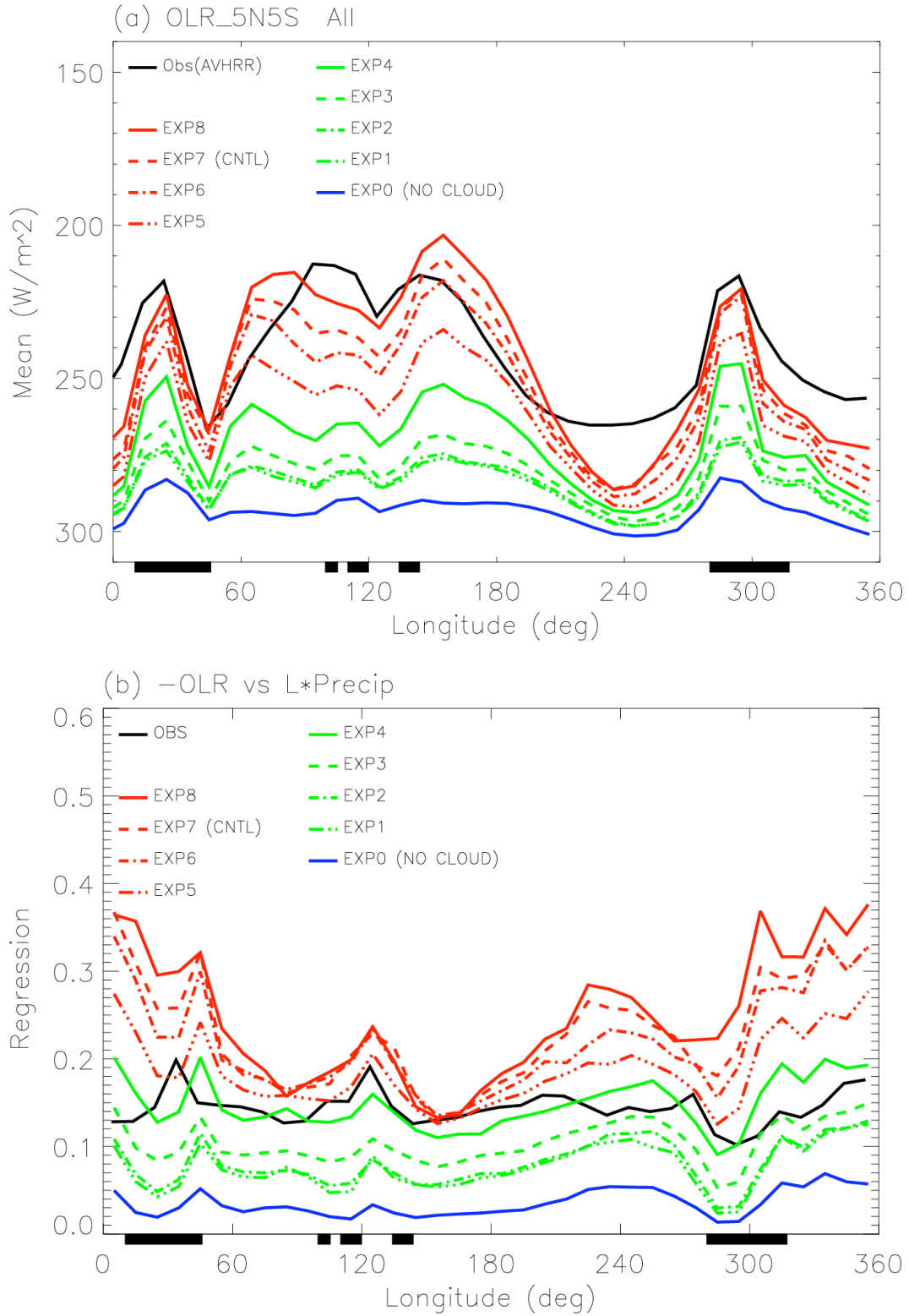


Figure 14. (a) Annual mean OLR, and (b) Linear regression of daily $-OLR$ vs precipitation along the equator averaged between 5N-5S for observation and model experiments. In (b) same unit is used for both variables so that the regression coefficient is unitless.